Analysis of EM wave scattering from asphalt and its application to automotive radar

Fan Lei

TU Delft

Analysis of EM wave scattering from asphalt and its application to automotive radar

Thesis report

by

Fan Lei

Thesis committee:

Supervisors:	Prof. DSc. Alexander Yarovoy,	TU Delft, supervisor
	MSc Wietse Bouwmeester,	TU Delft, daily supervisor
External examiner:	Dr.ir. Rob Remis,	TU Delft
Place:	Faculty of Electrical Engineering, Delft	
Project Duration:	September 15, 2022 - August 28, 2023	
Student number:	5402719	

Faculty of Electrical Engineering, Mathematics and Computer Science · Delft University of Technology

Abstract

The driver's safety is one of the problems that is considered by modern vehicle technologies. Many accidents occur due to extreme weather conditions, such as snow or freezing rain. Such weather causes decreases in the friction of the road surface, which cause danger for drivers in this kind of area. To improve the driver's safety, ADAS (Advanced Driver Assistance Systems) can be used to recognize different road surface conditions and warn the driver to avoid them. To do this, ADAS needs to perform classifications on the surface, and radars operating above 77 GHz have shown potential for this kind of task. The polarimetric information of the surface is needed as the prior knowledge for radar to perform the classification properly, which can be obtained from the scattering of the surface. The scattering properties of the asphalt surface at 76 GHz is a complex problem and it is difficult to have a comprehensive solution. In the existing research, there is no research that used a full-wave numerical approach with a simulation model for the kind of problem in the 76 GHz frequency band.

In this thesis, a numerical model is developed in the electromagnetic software suite FEKO to simulate asphalt surface scattering. The model considers surface roughness, dielectric medium, source polarization, and incidence angles for scattering from the asphalt surface. Based on the model simulations, statistical analysis is performed using the Monte Carlo method. The results of the model in the case of an RMS height of 2 mm and correlation length of 2mm show that for a very rough surface, the RCS of the surface decreases as the incidence angle is larger, and the value of the two polarization components is close to each other. By verifying the numerical model with SPM theory, it has been shown that the designed model can give accurate results in the designed scenarios, which proves that the designed model can be used for investigate rough surface scattering properties.

Acknowledgements

It has been two years since I began my studies at TU Delft. I gained a significant amount of knowledge throughout my time studying at this famous school, and I express my gratitude for the honor of being a student at TU Delft. During my education over the past two years, I would like to express my gratitude towards my supervisors, classmates, friends, and family members.

First of all, I would like to express sincere gratitude to my supervisor, Professor Yarovoy, and my daily supervisor, MSc Wietse Bouwmeester, for their invaluable guidance and support in proposing and supervising this interesting thesis topic, as well as for their constant help during every phase of this project. I sincerely appreciate their patience and kindness, which have helped me overcome every obstacle I've encountered while completing this project and writing the thesis.

I would also like to express my appreciation to Yue Chen and Bet Rufas Talamàs for their valuable contributions to the topic of research and for providing helpful details during my research for references.

Finally, I express my gratitude to my family and friends, whose constant support across physical distances and time zones.

Contents

Nomenclature

List of Abbreviations

ABS	Anti-lock braking system
ADAS	Advanced driver-assistance systems
AF	Array Factor
ANN	Artificial Neural Network
API	Application Programming Interface
BSC	Bistatic Scattering Coefficient
FDTD	Finite-Difference Time-Domain
FEKO	Feldberechnung für Körper mit beliebiger Oberfläche
FEM	Finite-Element Method
FIO	Factory Installed Option
FMM-FFT	Fast multipole method fast Fourier transform
GUI	Graphical User Interface
HDD	Hard Disk Drive
HPC	High-Performance Computing
IEM	Integral Equation Method
KA	Kirchhoff Approximation
KNMI	Royal Netherlands Meteorological Institute
MLFMM	Multilevel Fast Multipole Method
MoM	Method of Moments
PEC	Perfect Electric Conductor
PO	Physical Optics
PSD	Power Spectral Density
RCS	Radar Cross Section
RMS	Root Mean Square
SPM	Small Perturbation Method
SSD	Solid State Drive
TA	Tangent Plane
VRT	Vector Radiative Transfer

List of Figures

List of Tables

1 Introduction

This chapter introduces the background behind the project topic in Section 1.1, including the road surface condition classification and surface scattering problem. The review of the state-of-art is presented in Section 1.2. The problem statement is defined in Section 1.3 and the contribution of this project is summarized in Section 1.4. The main contribution of the project is to develop a numerical model of asphalt surface scattering and investigate the scattering properties of asphalt surfaces. Lastly, the structure of this thesis is explained in Section 1.5.

1.1. Background and motivation

Road safety is one of the problems that need to be considered for modern vehicles. The analysis of this problem involves many aspects, and one of the most essential aspects is the road condition. According to Royal Netherlands Meteorological Institute (KNMI), many accidents were caused by weather conditions like snow or freezing rain during the winter season [1]. This kind of precipitation is difficult to predict since it can be easily affected by the slightest change in temperature. To improve driving security, it is necessary for drivers to recognize the risky situation and react quickly.

The term advanced driver-assistance systems (ADAS) refers to the technologies that are implemented in modern vehicles to improve driving safety and comfort, including collision avoidance, blindspot monitoring, and Anti-lock braking system (ABS). For example, by giving warnings to the driver about hazardous areas with low friction or tuning the anti-lock breaking parameters of the system using ADAS, the risk of accidents due to dangerous road conditions can be reduced. In order to do this, the ADAS needs to be able to recognize different road conditions.

Modern vehicles can observe their surrounding environment using various methods, such as optical cameras, Lidar, radar, etc. An overview of different technologies used in road surface recognition is shown in Figure 1.1, in which several methods have been evaluated regarding operating conditions and measurement performance. Based on the comparison, it has been found that radar above 77 GHz seems to be the most promising method since it is independent of weather conditions and capable of long-range, high-resolution measurements. [2]

	Video	Lidar	Sonar	24 GHz Radar	>77 GHz Radar
Operation in rain, fog or snow	-	-	+	++	++
Operation at night	--	++	++	++	++
Range	++	+	-	+	++
Angular resolution	++	+	--	--	-
Range resolution	+	+	++	+	++

++ Ideally suited + Good performance
\- Feasible -- Impossible

Figure 1.1: An overview of different approaches for road surface classification

One way of using radar systems for road surface classification is to analyze the polarimetric information of the surface. The potential of using polarimetric radar for surface recognition has been demonstrated in early studies since the polarization state of the reflected signal is determined by the surface properties [3][4]. Furthermore, it

has been shown that the backscattering properties of surfaces can be changed by different surface conditions [5]. The measurement of the scattering matrix for different road surfaces in both laboratory and field experiments was executed by [6], their finding indicated that the backscattering properties of the road could be changed by water, ice, or snow in 24 GHz frequency band.

To classify the road condition using the polarimetric information, the scattering properties of the surface are needed as prior knowledge [7]. The scattered field from a surface can be influenced by many surface parameters, such as surface roughness, relative permittivity, conductivity, etc. Furthermore, the scattering properties of objects are also determined by incident angle, incident wave frequency, and polarization. With all of these uncertainties, it is difficult to obtain a general conclusion about the scattering properties of a surface under all circumstances. Therefore, to use automotive radar for surface classification, it is crucial to have an insight into surface scattering properties in the automotive radar operation frequency band, which is 76-80 GHz.

1.2. Overview of State-of-art

The goal of this project is to evaluate the scattering properties of electromagnetically rough surfaces, which can be used to classify the surface condition using polarimetric radar. In order to do this, the polarimetric information of the asphalt surfaces needs to be investigated using a certain method. The research starts with reviewing the existing studies that contributed to the analysis of asphalt surface scattering at 76-100 GHz. Then, the general existing approaches for rough surface scattering are reviewed to find a suitable one for this project. At last, a summary of the state-of-the-art is made, which includes the selection of the method and the novelty of this project.

1.2.1. Scattering from asphalt surfaces at 76-100 GHz

The investigation of the scattering properties of asphalt surfaces started a few years ago, and different approaches have been applied. Asphalt is a kind of material constructed from a mixture of small particles such as rocks and sand, and bitumen with air voids [7]. The size of the particles is comparable to or even larger than the millimeter wavelength at 76 GHz, so the volume scattering inside the medium also contributes to the scattered field. Some of the research used a hybrid approach to characterize the asphalt backscattering properties, in which the surface scattering is predicted by IEM and the dielectric characteristic of asphalt is obtained through experimental results to be used for the VRT (Vector Transfer Theory) to predict the volume scattering [7].

Experimental measurement is also one way to investigate the scattering properties. The backscattering coefficients can be computed by the polarized radar measurement. By measuring the angular response for asphalt and concrete surface of different roughness, it shows that the backscattering coefficient decreases as the incident angles become larger, and the horizontal and vertical components of the backscattering coefficient are different [8]. Another way of evaluating the backscattering properties is to measure the distribution of the backscatter. The radome-normalized backscatter shows different distributions for different surface conditions [9]. For high-frequency problems, many studies also used electromagnetic simulation software to find solutions. By building a numerical model, the scattering of rough surfaces can be simulated in given conditions. The investigation of the propagation and scattering of rough surfaces in the Terahertz band using full-wave simulation is done by using a model made of PEC (Perfect Electrical Conductor) [10][11][12]. By simulating a very thin surface with negligible thickness, the impact of the surface roughness on scattering in the Terahertz band can be studied.

1.2.2. Method of analysis for rough surface scattering

To analyze the scattering properties of random rough surfaces, different models have been developed in the past few decades. These models can generally be categorized into two types: analytical models and numerical models. To provide an insight into the scattering of the rough surfaces, analytical methods are proposed to find approximated solutions for random surfaces with fewer computational costs. The most commonly used methods include the Kirchhoff Approximation (KA), the Small Perturbation Method (SPM), and the Integral Equation Method (IEM).

Analytical models aim to develop an approximate model with less numerical complexity, while numerical models aim to find the exact solutions to Maxwell's equation. As technology grows, high-performance computers are now capable of running large computations and therefore become popular for solving this type of problem. The numerical methods aim to solve Maxwell's equations directly in their integral or differential form. Some of the methods are the Method of Moments (MoM), the Finite-Difference Time-Domain (FDTD), and the Finite-Element Method (FEM). The numerical approach can also be combined with the Monte Carlo method, which runs a large number of simulations to perform statistical analysis.

A. Analytical method: Small Perturbation Method (SPM)

The Small Perturbation method is one of the oldest methods in scattering analysis. It can be applied for slightly rough surfaces with a relatively small slope and surface height variations smaller than the incident wavelength [13]. The idea of SPM is to expand the scattered field to a perturbation series and find the solutions that satisfy boundary conditions. Therefore, the solution depends on the boundary conditions and the type of incident wave.

In this section, the formulation of the first-order solution for a problem with Dirichlet boundary conditions and scalar incident wave is discussed briefly [13].

First of all, the total field at the receiver is the sum of the incident field and the scattered field:

$$\psi(r) = \psi^{inc}(r) + \psi^{sc}(r) \tag{1.1}$$

in which r are the points on the surface, $\psi(r)$ is the total field, $\psi^{inc}(r)$ is the incident field and $\psi^{sc}(r)$ is the scattered field. For the scatterer that satisfies the Dirichlet boundary condition on h gives:

$$\psi(r)|_{z=h} = 0 \tag{1.2}$$

For a slightly rough surface, the surface height function $f(x, y, h)$ can be expanded to a Taylor series, and SPM assumes that the mean surface h of the rough surface is a plane at $z = 0$, then the surface height can be expressed as:

$$f(x, y, h) = f(x, y, 0) + hf_{,z}(x, y, 0) + \frac{h^2}{2} f_{,zz}(x, y, 0) + ... \tag{1.3}$$

where $f_{,z}$ are the derivatives. Scattered waves can be represented as a series using SPM:

$$\psi_{sc} = \psi_0^{sc} + \psi_1^{sc} + \psi_2^{sc} + ... \tag{1.4}$$

Take the first two terms of the surface height Taylor expansion in Equation 1.3 and the scattered field approximation in Equation 1.4, and take the expression of the total field in Equation 1.1 and substitute them all into Equation 1.2, the boundary condition becomes:

$$\psi^{inc}|_{z=0} + h\psi_{,z}^{inc}|_{z=0} + \psi_0^{sc}|_{z=0} + h\psi_{0,z}^{sc}|_{z=0} = 0 \tag{1.5}$$

By solving Equation 1.5, the zero-order solution of the scattered field $\psi_0^{sc}|_{z=0}$ and the first-order correction of to the scattered field $\psi_1^{sc}|_{z=0}$ can be obtained.

B. Analytical method: Kirchhoff Approximation (KA)

The Kirchhoff Approximation (KA) is also known as Tangent Plane (TA) or Physical Optics (PO) theory and it also can be referred to as the "high-frequency method". The idea of KA is to approximate the scattering of the rough surface, that the scattering of any point on the surface is considered a point scattering on the tangent plane at the same point, and the tangent plane is assumed to be an infinite smooth plane.

The formulation of the general form of the KA is explained in the following, the more detailed explanation can be found in [13]. First of all, the scattered field can be expressed as:

$$\psi^{sc}(\mathbf{r}) = \int_{S_0} [\psi(\mathbf{r}) \frac{\partial G(\mathbf{r}, \mathbf{r_0})}{\partial n_0} - G(\mathbf{r}, \mathbf{r_0}) \frac{\partial \psi(\mathbf{r_0})}{\partial n_0}] dS_0 \tag{1.6}$$

in which $\psi(\mathbf{r})$ is the total field and $G(\mathbf{r}, \mathbf{r_0})$ is the Green's function, S_0 is the surface of scatterer. These quantities in Equation 1.6 are known except for field and those terms are approximated by KA. By assuming a monochromatic plane incident wave $\psi^{inc}(\mathbf{r}) = e^{i\mathbf{k_{inc}} \cdot \mathbf{r}}$ and applying far field approximation $\mathbf{k}|\mathbf{r} - \mathbf{r_0}| \sim \mathbf{kr} - \mathbf{k\hat{r}} \cdot \mathbf{r_0}$, the integration is then converted to integration over the mean plane. Therefore, the general field Kirchhoff result can be written as:

$$\psi^{sc}(r) = \frac{-\mathsf{i}k\mathsf{e}^{\mathsf{i}kr}}{4\pi r} 2F(\theta_1, \theta_2, \theta_3) \int_{S_M} \mathsf{e}^{\mathsf{i}k\phi(x_0, y_0)} dx_0 dy_0 + \psi_e \tag{1.7}$$

where F is the angular factor and ψ_e indicates the "edge effects". The full expression for the variables can be found in [13]. The choice of the F depends on the choice of boundary, consequently, it varies in different literature. For an infinite, smooth planar surface, the KA can provide an exact solution. However, this assumption is impossible in

practical situations. In order to obtain accurate results, the following restrictions are proposed for the rough surface:

$$kr_c \cos^3 \theta_1 \gg 1 \tag{1.8}$$

where k is the wave number, r_c is the radius of curvature of the surface at a point on the surface, and θ_1 is the incident angle. The accuracy of the KA is limited not only by the surface properties but also by other scattering phenomena, since the original theory does not account for the multiple scattering and shadowing effects that occur when the incident frequency is higher and the surface is rougher. Therefore, the accuracy of KA is also limited by these parameters [13]. Additional terms such as the shadowing function were also proposed to extend the validation region of KA theory [14].

C. Analytical method: Integral Equation Method (IEM)

The Integral Equation Method (IEM) was proposed by A.K. Fung and G. W. Pan in 1963 to bridge the gap between the KA and first-order SPM [15]. The idea of this approach is to estimate the surface current by iterative technique, then the estimated surface current can be used for computing the scattered field. Their theory starts with the integral equation for the surface currents:

$$J(r) = 2\hat{n} \times H^i + \frac{1}{2\pi} \int \hat{n} \times [\nabla G \times J(r')] dS' \tag{1.9}$$

where $\hat{n}$ is the unit normal vector to the surface, H^i is the incident magnetic field and G is the Green's function. Considering a horizontally polarized incident wave:

$$E^i = \hat{y} E_0 exp(-jkx \sin\theta + jkz \cos\theta) = \hat{y} E_0 exp(-jk_x x - jk_z z) \tag{1.10}$$

where θ is the incident angle and k is the wave number in free space, and E_0 is the field amplitude. Let $n = \hat{n}/\cos\chi = -\hat{x}Z_x - \hat{y}Z_y + \hat{z}$ with $\cos\chi = [1 + (Z_x)^2 + (Z_y)^2]^{-1/2}$. The surface current in Equation 1.9 can be written as:

$$\frac{J}{\cos\chi} = 2n \times H^i + \frac{1}{2\pi} \int_S n \times \nabla G \times (\frac{J'}{\cos\chi}) dx' dy' \tag{1.11}$$

where Z_x and Z_y are the particle derivatives of the surface $z(x, y)$. In this equation, the first term represents the surface current density using KA and uses as the initial guess for the iterative process. The second term is a complementary term that can be simplified to remove the spatial variables. In this way, the total current density can be estimated, and then the scattered far field can be calculated [15]. The first term corresponds to single scattering, while the second term corresponds to multiple scattering.

Therefore, IEM can be used to analyze complex scattering problem which involves multiple scattering effects, while KA does not account for multiple scattering. Due to the limitation of computation, the problem needs to be restricted to make the resulting equation manageable [13]. Together with Vector Radiative Transfer (VRT) method, IEM can be used for the analysis of scattering properties of asphalt surface at 76 GHz, and the model is validated by experiment results [16].

D. Numerical method: Method of Moments (MoM)

The MoM method solves Maxwell's equation in integral form by discretizing the equation by expanding the surface current to a set of basis functions. This method forms a full matrix equation so that it can be solved by matrix inversion. Except for the basis functions, a set of weighting functions is used in this method as well. A brief explanation of the method is presented below [17]. Take the following integral equation:

$$\int_a^b dx' G(x, x') f(x') = c(x) \tag{1.12}$$

In which $G(x, x')$ is Green's function, $f(x)$ is the unknown variable, and $c(x)$ is the known variable in the integration domain. By expanding the unknown function $f(x)$ using basis functions:

$$f(x) = \sum_{n=1}^{N} b_n f_n(x) \tag{1.13}$$

and multiple with a set of weighting function $w_m(x)$, Equation 1.12 can be rewritten in matrix form:

$$\sum_{n=1}^{N} G_{mn} b_n = c_m \tag{1.14}$$

where $m = 1, 2, ..., N$, and

$$c_m = \int_a^b dx w_m(x) c(x) = \langle w_m, c \rangle \tag{1.15}$$

$$G_{mn} = \int_a^b dx w_m(x) \int_a^b dx' G(x, x') f_n(x') = \langle w_m, G f_n \rangle \tag{1.16}$$

Equation 1.14 is a full matrix equation, in which the unknown surface current $f(x)$ can be solved based on the weighting functions, from which the scattered field can be calculated [17]. Therefore, the choice of the weighting function determines the accuracy of the solution. Two common choices of the weighting functions are Galerkin's method and the point matching method.

The advantage of the MoM is that it is easy to implement. However, due to fact that the general MoM solves the full matrix equation, the computational complexity of the method depends on the matrix dimension N and it grows rapidly with this number. Many techniques have been proposed to reduce the computation cost of these equations [17]. For example, the MLFMM (Multilevel Fast Multipole Method) is one of the fast methods for electrically large systems. The MLFMM finds quick solutions for large systems by approximation of the matrix elements' coupling. It solves the large system matrix by computing the coupling between a group of matrix elements instead of the coupling between all matrix elements. Each element group contains a group of matrix elements and the coupling of one element in the group to the other element group is approximated by the coupling between the two groups [18]. In this way, the number of unknowns of the matrix is reduced and therefore the computation efficiency is improved.

E. Numerical method: Finite-difference time-domain (FDTD)

The FDTD method was first introduced by Kane S. Yee to solve the differential form of Maxwell's Equation in the time domain [19]. The idea of this method is to use finite difference equation to approximate the derivative operator in Maxwell's Equations. These difference equations are discretized in space and time and formulated based on boundary conditions. For a grid in space, a set of nodes are selected and the electromagnetic field on these nodes can be calculated by the differential equations [19]. The iterative scheme is applied to the calculation, the initial values of the fields are derived from the incident wave, and the field values of a given time step are then calculated based on the values of the previous steps. In this way, the electromagnetic wave's propagation in the time domain can be computed.

One of the advantages of the FDTD is that the scattering properties for different frequencies can be obtained simultaneously. In addition, the matrix inversion process is eliminated compared with other methods [20].

F. Numerical method: Finite Element Method (FEM)

For the case with an inhomogeneous medium, FEM is more suitable than other methods [21]. For a multi-layer surface, by dividing the scattering region into several parts based on the specific problem, FEM can find the solution of the total field in the inhomogeneous region.

A solution of a combined random rough surface is provided by diving the problem into two regions [21]. Region I consist of a homogeneous region above the highest point of the rough surface, and region II consists of the inhomogeneous region of the rough surface. The scattered field in region I is solved by expanding it in upward traveling Floquet modes. The FEM is applied to region II by dividing this region into first-order triangular elements, which are called finite elements. The total field in region II can be expressed as a linear combination of the modal field within each element. The solution for the whole system is the combination of two regions which also satisfies the boundary conditions between the two regions. In this way, the FEM is able to calculate both surface scattering and volume scattering of the surface.

Except for the capability of solving the inhomogeneous problem, another advantage of the FEM is that it requires less computational time and memory than other methods. In the region where FEM is applied, the height in this simulation is significantly smaller than the total surface length so it costs less computation time to discretize the region. Furthermore, the matrix in the linear equation is symmetrical and only half of it needs to be stored, which results in less requirement for computational memory [22].

1.2.3. Summary of different method

A summary of the pros and cons of two different types of approaches is presented in Table 1.1. The analytical methods have been developed for many years and many studies have proposed validated models to predict rough surface scattering. In the known validation regions, it could provide accurate predictions and they can be helpful to quantitative analysis. But the validation region of the analytical models is ambiguous and difficult to determine [23]. The accuracy of the result is also restrained by several criteria. For example, results become less accurate when the grazing angle is small. By using additional terms like shadow function the precision of the results can be improved [14]. However, the application of analytical models for complex problems is still limited.

On the other hand, numerical methods can provide precise solutions for complex problems since it solves Maxwell's Equations directly. It can be applied to various kinds of problems, such as scattering problems on the surface with buried objects and multi-layered rough surfaces [9][24]. The requirement for computational resources using numerical method increases as the system model complexity increases. The development of high-performance computers allows the numerical model to be solved with less time. Therefore, the numerical method is preferable to the analytical methods for practical problems with complex surfaces.

Method	Advantages	Disadvantage
Analytical methods	1. Provide accurate results within the known validation region. 2. Requires fewer computational resources than the numerical methods.	1. The accuracy of the prediction depends on the criteria, such as the surface RMS heights and slope, and the incident angle. 2. Difficulty in the determination of validation region.
Numerical methods	1. Provide accurate results with less dependence on conditions. 2. Capabilities of solving complex problems, such as scattering problems of the surface with buried objects	1. The requirement for computation resources increases with the complexity of the model. 2. The accuracy depends on the mesh grid size.

Table 1.1: Summary of two methods

By viewing the existing studies, it can be concluded that the scattering from asphalt surfaces at high frequencies is a complex problem for which it is difficult to have a comprehensive solution. The composition of asphalt also varies for different applications, so the dielectric properties of asphalt also vary between research [7]. In addition, many analytical studies focus on a range of incident angles, while the numerical model from full-wave simulation could provide results in more different incident angles. The parameters of the numerical model can be adjusted and resolved by the simulation software to obtain various results for different conditions. Therefore, the numerical method is more suitable for this project.

Among all of the numerical methods, the principle of the FEM and FDTD algorithms requires that the model is meshed in volume to find the solution, while the MoM only meshes the model surface to estimate the surface current and calculate the scattered field. For this problem, the dielectric medium is assumed to be homogeneous, and MoM appears to be more computationally efficient. For electrically large systems, it is reported that the multilevel fast multipole method (MLFMM) is found to be more efficient than the fast multipole method fast Fourier transform (FMM-FFT) method for solving scattering problems with large roughness [25]. In conclusion, the MoM-based solver with the MLFMM algorithm is the most suitable for this project.

From the literature review of the existing studies, many studies have investigated the problem of asphalt scattering [5][9][16]. It is reported that the backscattering coefficient of the surface decreases when the incident angle is increasing, and it is different for different polarizations and surface conditions [8]. But they were using either analytical or experimental approaches and none of the research used a numerical approach.

There are a few studies that have investigated asphalt surface scattering using numerical approaches. However, most of the research focuses on problems in a higher frequency band than 76 GHz, and some of the research focuses on the analysis of surface scattering of the rough surface without the surface thickness or dielectric constant, and there is no statistical analysis as well [10].

To the best of the author's knowledge, there is no existing research that used numerical model simulations for evaluating the asphalt surface scattering properties in the 76 GHz frequency band, and there is no existing similar numerical model that considers comprehensively the physical parameters of the asphalt surface, such as the surface thickness and the dielectric constant of the asphalt. Therefore, the novelty of this project is to develop a new numerical approach for the asphalt scattering problem, and the model includes several aspects of surface scattering instead of only surface roughness. Furthermore, by applying a Monte Carlo method, this project also performs a statistical analysis of the results.

1.3. Approach

In this project, first of all, a numerical model of asphalt surface scattering at 76 GHz will be developed in the simulation software FEKO (Feldberechnung für Körper mit beliebiger Oberfläche). In this project, the asphalt mixture is assumed to be a homogeneous medium. Then, the scattering properties will be analyzed based on the results produced by the designed numerical model. Previous studies have investigated the dielectric properties of the asphalt material and the scattering properties of a PEC rough surface, which has similar roughness to asphalt surfaces [26][27]. The work of this project is formulated based on their contributions.

The development of the numerical model starts with the design of the rough surface model and the incident source. Based on the designed model, the simulation is configured in the FEKO and the scattering of a single deterministic asphalt surface can be simulated. To obtain a statistical result, the number of realizations is decided, this number of random surfaces with the same characteristics is simulated, and the results are averaged. The scattering properties will be investigated in terms of the scattered far field and RCS (Radar Cross Section), and how they are influenced by the incident angle and surface characteristics.

1.4. Contribution of the Research

The main contributions of this thesis project are summarized below:

- A novel numerical model is developed to simulate the scattering from the asphalt surface at 76 GHz. This model is designed with thickness to consider the impact of both the surface roughness and wave penetration of a dielectric medium on the scattering properties.
- For the first time, scattering from the surfaces with electrically large roughness is studied. The investigation includes the aspects of source polarization, incident angle, and surface RMS height.
- A statistical analysis of the scattering characteristic of the asphalt surface is performed. The scattering properties are analyzed in terms of the averaged results to have a statistical result. The scattering properties are evaluated by the averaged far field pattern and the averaged RCS, which can be used for road surface classifications with automotive radar.
- A multilayer model consisting of water and an asphalt layer is designed to study the impact of an additional dielectric medium layer on the asphalt scattering properties.

1.5. Outline of the Thesis

The structure of this report is explained in this section. The first chapter introduced the background information and the motivation of this project, the review of state of the art, then the problem approach is brought up based on the review followed by the contribution of the research. Chapter 2 introduces the computational model, including the generation of the rough surface model, the section of the surface model and configuration in FEKO, followed by the simulation procedure in different computer clusters, and the post-processing of the simulation results. At last, the limitations of the designed model are explained. In Chapter 3, different scenarios are designed to investigate the scattering properties of the rough surface, this is done in the aspect of the RMS height and the incident angles with both horizontal and vertical incident polarization. The results are evaluated in terms of the averaged far field pattern and the four polarimetric components of the BSC (Bistatic scattering coefficient) and RCS. This is followed by the explanation of the multilayer model in Chapter 4, the multilayer model is built based on the design of the single-layer model to provide an insight into the impact of an additional dielectric medium layer. The development

of the model and results are presented in this chapter. Chapter 5 explains the verification of the single-layer model by comparing the simulation result to the SPM theory. The results show that the model has good agreements with the SPM prediction with limitations. At last, the conclusions and recommendations for further research are derived based on the results in Chapter 6.

2

Computational model

In this chapter, the development of the computational model for asphalt surface scattering is explained. It starts with simulating a single piece of asphalt surface in FEKO, which includes generating the asphalt surface, selecting the incident source, and determining the size of the model. The procedure for generating a rough surface model is explained in Section 2.1. Followed by studies of the influence of incident source and surface dimension in Section 2.2 and 2.3, then the parameters for the surface size and simulation parameters are set and tuned in Section 2.4. Subsequently, the procedure expands to simulate a set of surfaces with the same characteristics to obtain a result set. This step involves the use of an HPC (High-Performance Computing) cluster. The workflow for simulating dielectric surfaces using FEKO is explained in Section 2.5. The processing of the simulation results is presented in Section 2.6. At last, the limitations of the computational model are analyzed based on the simulation result in Section 2.7.

2.1. Rough surface generation

The scattering of the asphalt surface is determined by the geometrical properties of the surface and the dielectric properties of the asphalt mixture. This section explains the generation of a rough surface with the same statistical geometrical properties as an asphalt surface, as well as the preparation for model import in FEKO. To obtain a comprehensive study, a group of surfaces needs to be randomly generated with the designed parameters and also follow the same height distribution as the real asphalt surface.

The first step is to extract the properties of the real asphalt surfaces. By sampling the CT scans of asphalt surfaces, the height distribution of the surface can be obtained. The PSD (Power Spectral Density) function of this distribution can then be calculated by the Fourier transform. According to the Wiener-Khinchin theorem, the correlation function of the random surface is related to the PSD function. According to the results, the asphalt surface height distribution fits into an exponential distribution, and the correlation function is a Gaussian distribution [27]. The RMS (Root Mean Square) height σ and the correlation length L of the surfaces are both 2 mm.

The generation of synthetic surfaces involves spatial filtering and probability transformation. For a random distribution X fol, the CDF of X follows a standard uniform distribution:

$$P(Y \leq y) = P(F(x) \leq y) = P(x \leq F^{-1}(y)) = F(F^{-1}) = y \tag{2.1}$$

in which $Y = F(x)$ is the CDF of X, $F^{-1}(x)$ is the quantile function of X. A standard uniform distribution Y can be transformed to an exponential distribution by the logarithm $Z = \frac{1}{b} \ln(\frac{Y}{a})$:

$$P(Z \leq z) = P(\frac{1}{b} \ln(\frac{Y}{a}) \leq y) = P(y \leq ae^{by})) = ae^{by} \tag{2.2}$$

In this way, a surface with a uniform distribution of surface heights can be converted into one with an exponential distribution. This principle is used in the following procedure to generate a synthetic asphalt surface model.

An overview of the surface generation procedure is presented in Figure 2.1. The procedure begins with the design of a spectral filter, which is based on the Gaussian autocorrelation function:

$$ACF = exp(-(\frac{\sqrt{x^2 + y^2}}{L})^2) \tag{2.3}$$

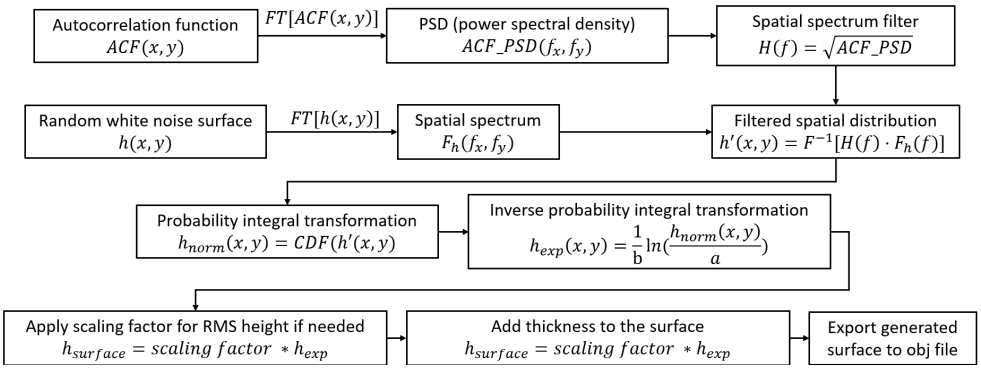

Figure 2.1: Procedures of generating a rough surface model

Here x and y are the grid points in the X-Y plane, L is the correlation length. This filter is then transformed to the spectral domain by the Fourier transform to be used as a spectrum filter. The second part of the procedure starts with creating a random white noise surface. The created surface is transformed into the spectral domain by the Fourier transform, so it can be filtered by the spectrum filter to have the desired spectrum and autocorrelation function.

After adjusting the spectrum of the surface, the height distribution of the filtered surface needs to be adjusted to an exponential distribution by probability transformation. The uniform distribution can be derived from the filtered surface using the probability integral transformation, as shown in Equation 2.1. Subsequently, the obtained uniform distribution is transformed to an exponential distribution by the inverse probability integral transformation, as shown in Equation 2.2.

The adjusted surface now follows the same height distribution as asphalt surfaces, as well as the same RMS height and correlation length. For further analysis, the RMS height can also be adjusted by applying scaling factors. This allows for the generation of an arbitrary surface with the specified surface dimension, correlation length, and RMS height, which has the same properties as the asphalt surface. The surface is subsequently assigned a specific thickness. At last, the surface is represented by mesh triangles and exported as a wavefront obj file.

In Blender, the units and orientation of the model are adjusted to match the settings in the CADFEKO environment, and the file format is converted to an STL file so that it can be imported as a mesh file into CADFEKO. An example of the generated surface is demonstrated in Figure 2.2. Figure 2.3 and Figure 2.4 indicate that the generated surface has a similar Gaussian height distribution and the same normalized autocorrelation function as the asphalt surface.

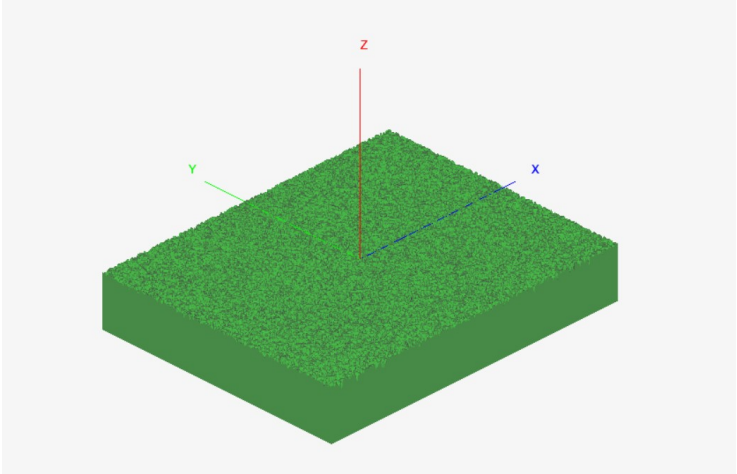

Figure 2.2: An example of the generated model in CADFEKO

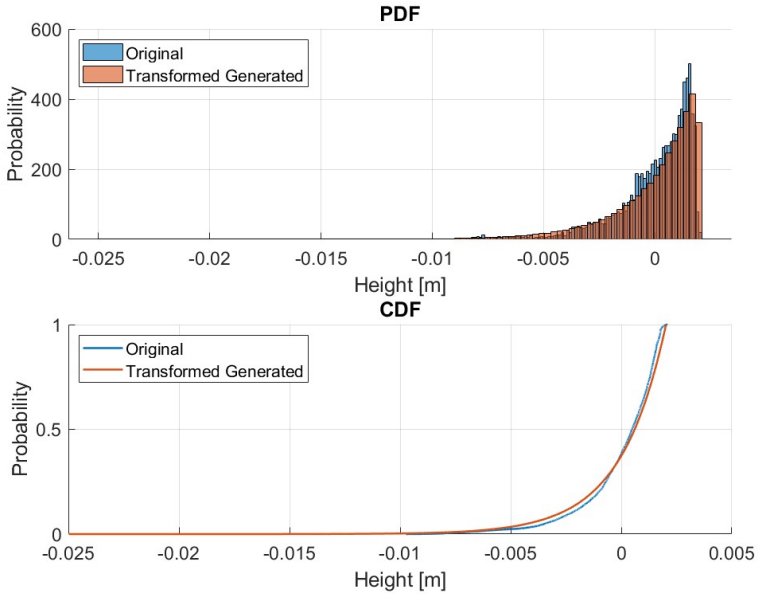

Figure 2.3: The comparison of the PDF and CDF of the original asphalt sample and the generated surface

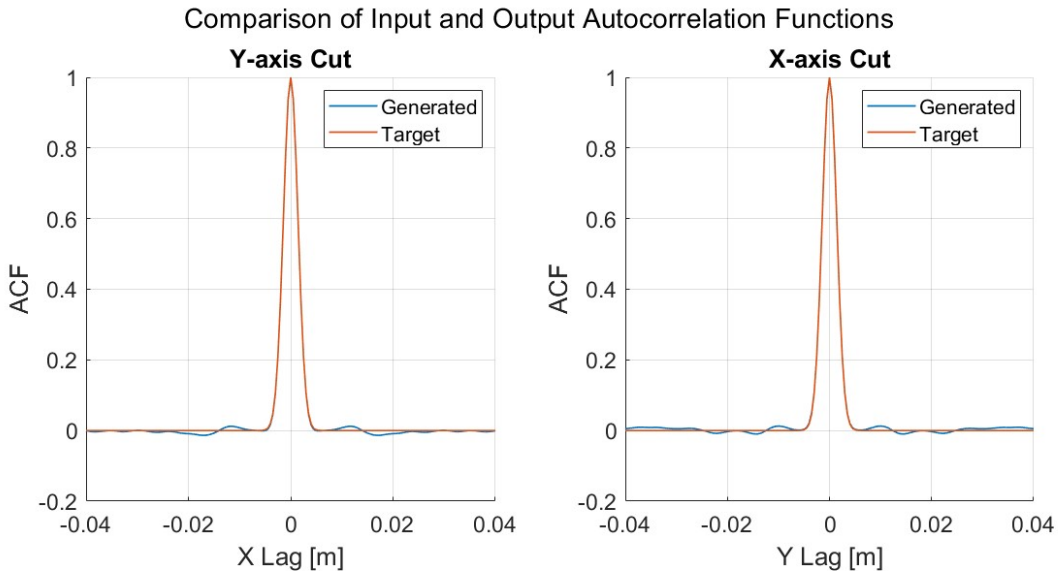

Figure 2.4: The comparison of the autocorrelation function of the original asphalt sample and generated mode

2.2. Selection of sources

In this section, the selection of the source is explained. In order to analyze the scattering properties, it is essential that the scattered field is not interfered with by the finite size of the simulation model. When a plane wave is incident on a finite surface, the magnitude of the surface current peaks at the edge of the surface [28]. This edge effect would cause additional side lobes in the far field pattern due to diffraction, interfering with the scattering properties analysis.

An alternative option is to use a tapered incident wave to avoid illumination at the edge. A Gaussian weighting is one of the commonly used tapering for the incident source [28][29][30]. However, such a tapered incident wave from the numerical methods is realized by the integral of a set of plane waves, which is computational intensive for full-wave simulation approach [31]. Consequently, an antenna model with a low side lobe level radiation is used as the incident source. At first, a horn antenna was previously used as the incident source [27]. The dimension of the horn antenna is shown in Figure 2.5 and the radiation pattern of the antenna is shown in Figure 2.6, where it can be observed that the side lobe level is very high. The presence of the side lobe will interfere with the surface and induce additional surface currents, which leads to the scattering from both the main lobe and the side lobe of the source appearing in the scattered field.

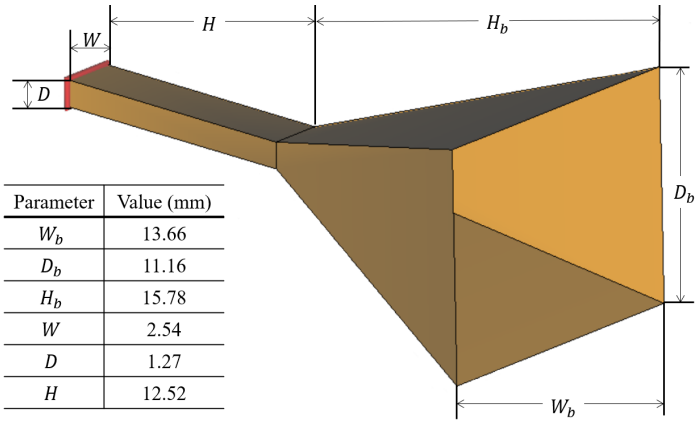

Parameter	Value (mm)
W_b	13.66
D_b	11.16
H_b	15.78
W	2.54
D	1.27
H	12.52

Figure 2.5: The dimension of the horn antenna

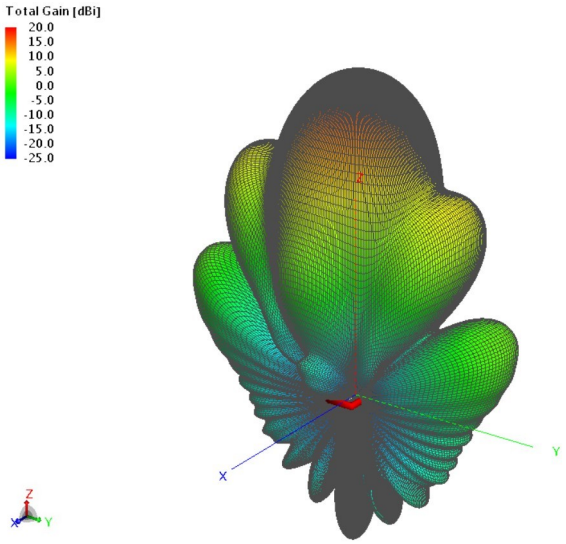

Figure 2.6: The radiation pattern of the horn antenna at 76 GHz

To eliminate the side lobe effect, another tapered source was designed to suppress inference from both the edge effect and the side lobe [26]. It is a two-dimensional binomial dipole array with seven elements in each dimension and a half-wavelength spacing between the elements. The Array Factor (AF) can be written as:

$$AF = 2a_1 \cos(3kd\cos\phi) + 2a_2 \cos(2kd\cos\phi) + 2a_3 \cos(kd\cos\phi) + a_4 \tag{2.4}$$

in which a_i is the magnitude of the element. In this case, $a_n = (1, 6, 15, 29)$, k is the wavenumber in free space, d is the spacing between the elements, and $d = \frac{\lambda}{2}$ where λ is the wavelength. To prevent backward radiation, a PEC reflector is placed behind the array at a distance of $\frac{\lambda}{4}$. The radiation pattern of the source is shown in Figure 2.7.

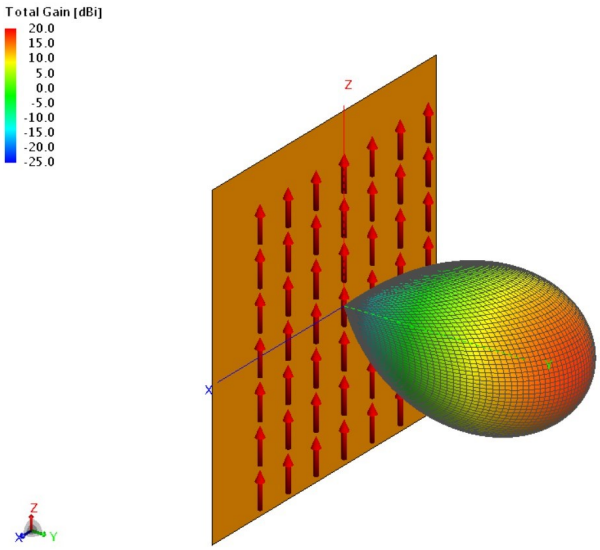

Figure 2.7: The radiation of the dipole array at 76 GHz

The comparison between the two incident sources on a flat asphalt surface is shown in Figure 2.8. The result shows that the scattered field caused by the side lobes of the source is suppressed when the binomial array source is used. The side lobe caused by the edge effect appears in the direction of 100°, proving that the dipole array source also suppresses edge diffraction.

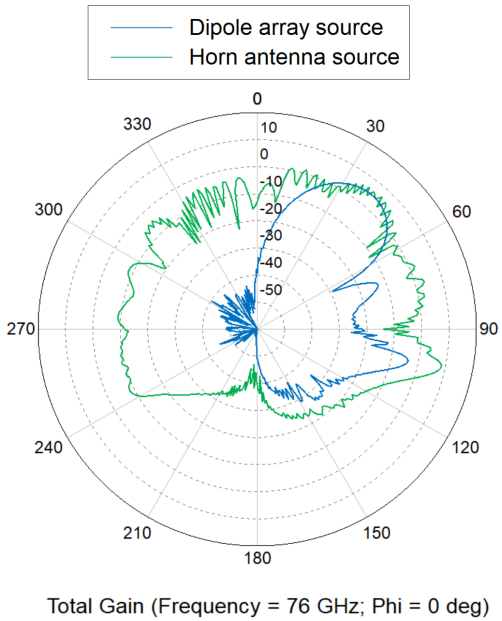

Figure 2.8: The far field pattern of two types of sources incident on the flat dielectric brick with Phi = 0°

2.3. Effects of surface dimensions

In this section, the influence of surface size is investigated to select a suitable size for the surface model. First, a group of asphalt models with different sizes is simulated to find the effects of the surface size. Then, the thickness of the surface model is investigated.

2.3.1. Effects of surface size

As demonstrated in Figure 2.8, using a tapered source for flat surfaces can reduce diffraction at the edge. For a relatively small surface, the diffraction appears to be larger. To suppress the edge effect of the rough surface further, the size of the surface needs to be increased. On the other hand, the size of the model is constrained by the computer's memory capacity. A large model could require significant computational resources and memory on the computer, thereby decreasing the simulation's efficacy. As a result, the brick size can only be as large as possible while still requiring a reasonable amount of computational resources and time. A test is designed to find out the optimal surface size.

The previous research has succeeded in simulating a PEC rough surface with a size of 400 mm squared and 40 mm thickness [26]. These simulations were run on a computational server. In this project, to improve efficiency, simulations will be run on an HPC cluster named DelftBlue, which has more computational power than the server. Considering that the source is incident along the x-z plane, the length of the surface affects the scattering more significantly than the surface width. Therefore, the test starts with the same size of 400 mm square and increases only in length by 20 mm per step until it reaches 500 mm, and the simulation results are shown in Figure 2.9.

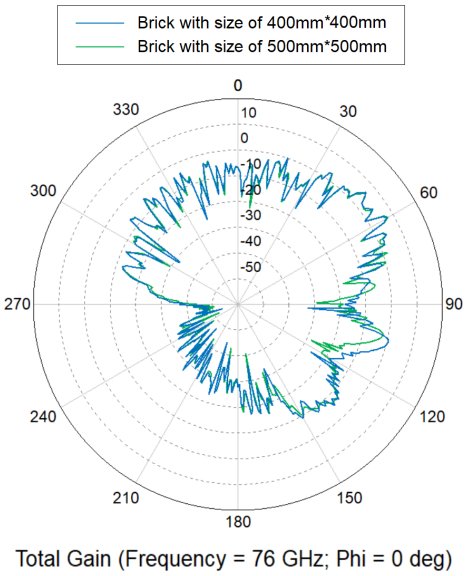

Figure 2.9: Far field of the rough asphalt surface with two different sizes

From Figure 2.9, it can be found that the diffraction on the edge appears as a side lobe around 100°, and this side lobe decreased for bricks with 500 mm.

In the software aspect, FEKO discretizes the model by mesh and computes the outputs based on the generated mesh model. The mesh consists of a group of triangles, therefore, the solution accuracy and the computational requirement depend on the number and size of the triangle elements. The number of unknowns required to solve the system is determined by the number of triangles. For a large number of triangles, the model solution can be precise at the cost of large computational requirements. For different rough asphalt brick sizes, the change in the number of triangles is shown in Figure 2.10. As the size of the model increases, the number of meshed triangles increases, which leads to a large number of unknowns that need to be solved. Due to the fact that more unknowns require more computational resources, a surface larger than 500 mm exceeds the available computational resources for this project, and the frequency of the software's internal error increases as the model size increases. Consequently, the surface size cannot be increased further. The details about the final selection of the surface size are explained in Section 2.4.

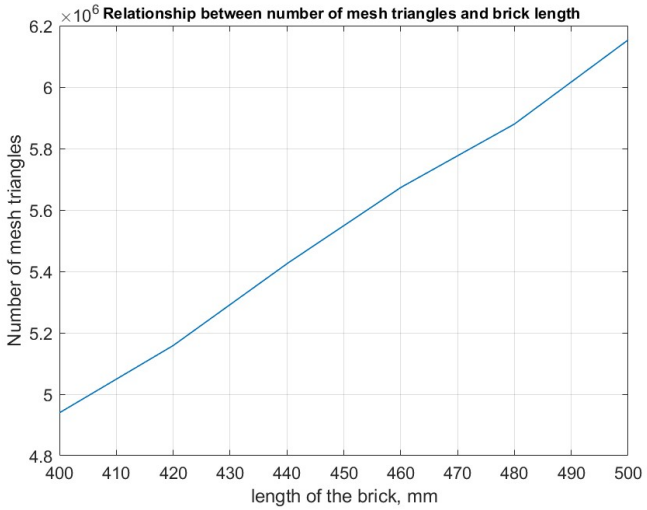

Figure 2.10: The number of triangles in different lengths of models

2.3.2. Effects of brick thickness

Another aspect of the model size is the thickness of the brick. The PEC boundary fully reflected the wave in the previous PEC model in [26], so the model thickness did not affect the total field. In contrast, the incident field penetrates the asphalt brick and contributes to the total field in the dielectric case. For a dielectric object, the incident wave penetrates into the medium, and propagates inside, and reflects from the lower boundary, which influences the backscattered total field. The influence from the field inside can be reduced by increasing the thickness, which increases the propagation loss. Figure 2.11 shows the far field result of the flat asphalt surfaces with two different thicknesses. As the thickness increases, the lobe in the direction from 120° to 150° is suppressed, which indicates that the interference of the propagation through the lower boundary is reduced.

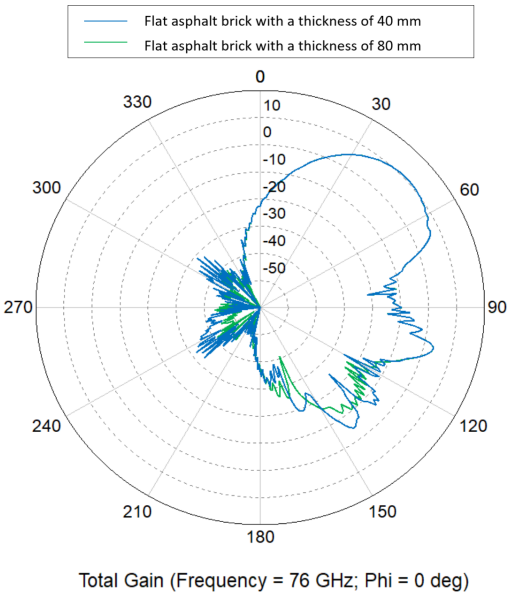

Figure 2.11: The far field of the same rough surface with two different thicknesses

2.4. Selection of surface model and simulation parameters

In this section, the finalized selection of the parameters of the simulation is explained. This includes the selection of the thickness and size of the brick based on the investigation in Section 2.3, and the equivalent source format of

the designed dipole array source. To obtain a statistical result, the Monte Carlo method is applied, and the details of this method are explained in the last subsection.

2.4.1. Brick size

The simulation results in the earlier sections prove that the edge effects and interference of the penetrating field can be suppressed by increasing the size and thickness of the surface. By combining the conclusions from the two experiments, the dimensions of the brick are determined to be 500 mm in length, 400 mm in width, and 80 mm in thickness. Although there is room to further increase the size if only the computational requirements are considered, other factors must also be taken into consideration. The simulation time is the first issue. The time cost is determined by the hardware, and for the selected brick size and the computer used in this project, it takes an average of about 5.76 hours to run a simulation. In addition, the average total time for one simulation rises to 18 hours after adding the average pending time on the HPC cluster, and the fact that a large number of simulations need to be run for each source and surface profile parameter set to obtain a statistical analysis. The second issue is the internal errors in the simulation software, FEKO. For example, during the testing simulations, some of the simulations required an abnormally large amount of memory that exceeded the hardware capability of HPC cluster and failed due to a memory shortage. This error happens more frequently as the model size increases. The reason for this unreasonable memory requirement remains unsolved.

2.4.2. Equivalent source

To reduce the model complexity, FEKO offers the option to export the results as equivalent source files for use in other simulations. There are three types of export modes of source: near field, far field, and spherical mode source, each of which applies a different approximation. The use of the source depends on the model definition and the approximation conditions of the equivalent source. For this project, the distance designed between the source and the center of the surface is $100\sqrt{2}$ mm. As a result, the incident point on the surface is located in the far field region of the source. However, the surface is not fully located in this region. The shortest distance between the source and the surface with a 45° incident angle is 100 mm and it is in the near-field region. In this case, the far field equivalent source may not provide an accurate result. To investigate this problem, a comparison between the two types of equivalent sources and the original array source on the flat surface is shown in Figure 2.12.

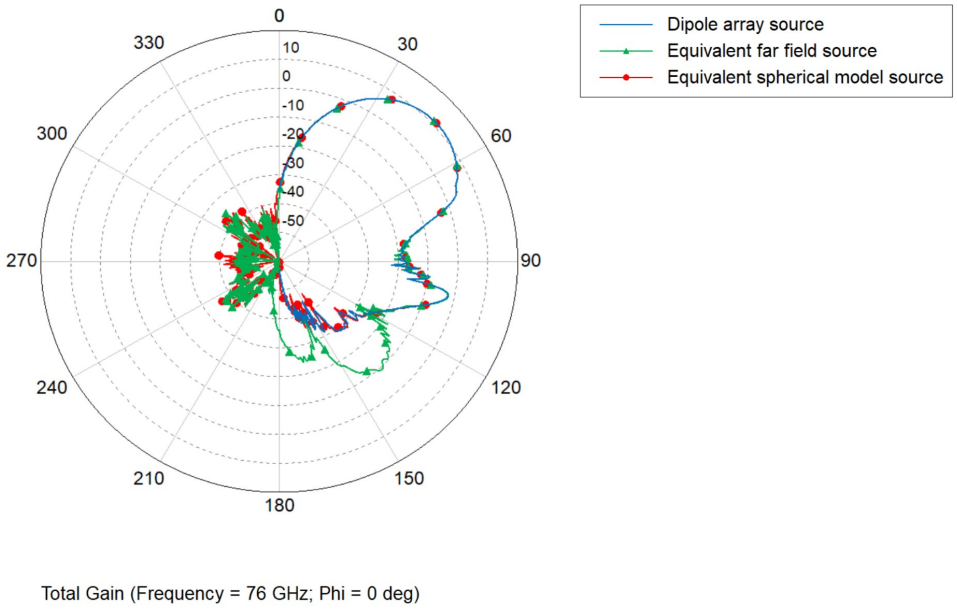

Figure 2.12: Far field of three different types of the source incident on the same size of flat asphalt brick

This figure shows an additional lobe beneath the brick when the far field source is used, which could be explained by the distance to the surface not completely satisfying the far field approximation condition. Meanwhile, the spherical mode source appears to be very close to the original array. Since the spherical mode source is independent of the far field approximation condition, it provides a more precise prediction of the result.

2.4.3. Monte Carlo method and number of realizations

As the simulation solves one deterministic model at a time, to analyze the characteristics of the surface with a random distribution, the Monte Carlo method is applied. The Monte Carlo simulation is one of the essential methods for quantitative studies. It can realize random objects or processes that arise 'naturally' or 'artificially' as part of the modeling of a practical system [32]. The idea of the method is to repeat the simulations many times to obtain quantitative results, and it has been widely used for the analysis of scattering problems in the numerical approach. To study the characteristics of scattered fields of random surfaces, a set of surfaces is generated individually, and their results are averaged to acquire a statistical result of surface scattering properties.

The accuracy of the Monte Carlo method is determined by its convergence. A large number of simulations can provide more accurate results, whereas some important features might be neglected with a smaller number of simulations. The required number of simulations depends on the required convergence and the research objective. The average far field is obtained by calculating the average value on each position of the field. The averaged results from different numbers of realizations are shown in Figure 2.13. As the number increases, the result converges to a steady state. The average gain at 315° for different numbers of realizations is shown in Table 2.1. The difference in average gain between one and ten realizations is 4.32 dB, the difference between 10 and 20 realizations is 2.04 dB, and the difference between 20 and 30 realizations is 1.25 dB. The decrease in the difference between the averaged results shows that the result starts to converge with 10 simulations and appears to be stable with 30 realizations. As a result, the number of realizations is decided to be 30.

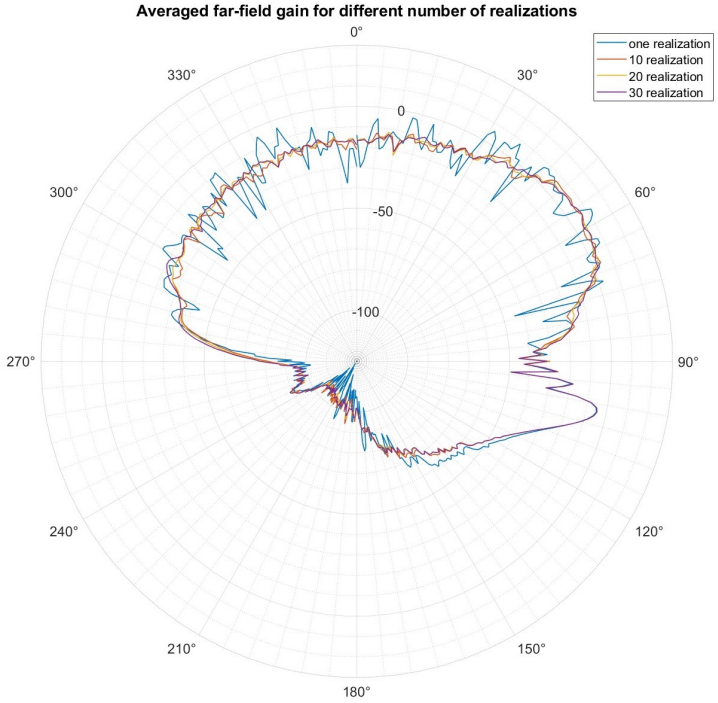

Figure 2.13: Average far field result from different numbers of realizations

Table 2.1: Average gain at 315° for different number of realizations

Number of realizations	1	10	20	30
Average gain (dB)	-19.58	-23.90	-21.86	-20.50

2.5. Simulation of dielectric surfaces using FKEO

In this section, the simulation setup on the different computational environments is explained. The simulation is first set on a computational server, followed by simulations on the HPC cluster.

2.5.1. Simulation using a computational server

In this section, the process of simulating one piece of the rough asphalt surface using the MS3 server is explained. The detailed configuration of MS3 is shown in Table 2.2 [33].

Table 2.2: Configuration of MS3 server

Hardware category	Number	Configuration
Processor Kit	1	DL360 Gen10 Intel Xeon-Gold 6230 (2.1 GHz/20-core/125 W)
FIO (Factory Installed Option) Processor Kit	1	DL360 Gen10 Intel Xeon-Gold 6230 (2.1 GHz/20-core/125 W)
Registered Smart Memory Kit	8	32GB (1x32GB) Dual Rank x4 DDR4-2933 CAS-21-21-21
Wty Digitally Signed Firmware HDD (Hybrid Disk Drive)	2	4TB SATA 6G Midline 7.2K LFF (3.5in) SC
Wty Digitally Signed Firmware SSD (Solid State Drive)	2	480GB SATA 6G Read Intensive LFF (3.5in) SCC

An overview of the workflow for setting up the simulation is presented in Figure 2.14. After creating and converting the generated model. The first step in CADFEKO is to import the generated rough surface model. In the CADFEKO modeling environment, the imported model only contains its geometrical properties. To further define it as a dielectric surface, the imported model's dielectric properties need to be modified. The dielectric properties of the asphalt were investigated in the previous project, in which the relative permittivity of the asphalt was determined to be 4, and the conductivity of the asphalt was found to be 0.767 S/m [27]. The corresponding dielectric constant can be computed by:

$$\tan\delta = \frac{S}{\omega\epsilon_0\epsilon_r} \tag{2.5}$$

where:

$\tan\delta$: medium loss tangent,

ϵ_0: free space dielectric constant,

ϵ_r: real part of the dielectric constant of the medium,

S: conductivity of the medium.

ω: angular frequency, with $\omega = 2\pi f$.

In this case, the complex dielectric constant of the asphalt is $\epsilon_{asphalt} = 4 - j0.181$. On the mesh setting tab, the properties of the imported model can be modified. The front medium is set to free space, the back medium is set to asphalt, and the face medium is set to the dielectric boundary. Then, the equivalent source can be added. The equivalent source file is imported into the environment and then a spherical source is defined by selecting the imported field file and altering the source's orientation.

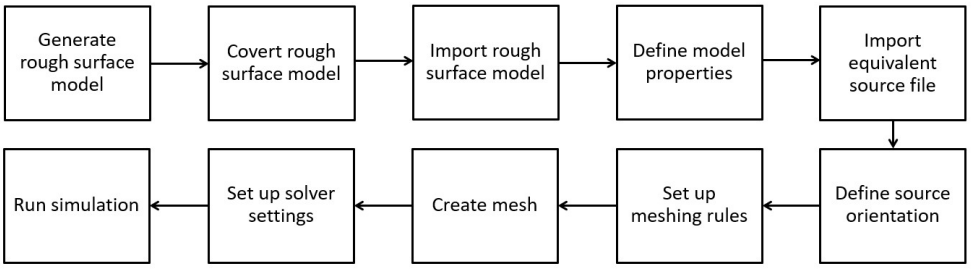

Figure 2.14: General workflow of setting up a simulation in MS3 server using GUI (Graphic User Interface)

After the model and source are imported, the imported geometrical model needs to be meshed. This is because FEKO computes solutions based on the mesh model, which is the discretization of the geometric model [34]. After enabling the re-meshing option, the software provides an automatic meshing function for the user to create a mesh model based on a frequency input. The automatic meshing provides three options for mesh type: fine, standard, and coarse. To reduce the computational requirement, the meshing rule for this project is set to coarse, which indicates that the size of the mesh is $\lambda/8$ [34].

Regarding the solver aspect, FEKO provides many kinds of numerical solvers. From the review in Section 1.2.3, the MLFMM (Multilevel fast multipole method) is the most suitable algorithm for this type of model, therefore it is

selected. To improve the computational efficiency, an advanced setting for the solver is used, namely the iterative solver with the SPAI (Sparse approximate inverse) preconditioner selected to reduce the amount of required memory.

2.5.2. Simulation using HPC cluster

After successfully simulating a single brick, the procedure then moves on to generate a group of results so they can be averaged. The batch simulation is performed on DefltBlue, which is the supercomputer at TU Delft that is designed for solving complex problems that require extensive computing power. The detailed configuration of Delftblue is shown in Table 2.3 [35]. The cluster consists of three types of compute nodes with different configurations of memory or GPU cards. The jobs uploaded on DelftBlue are managed by the Slurm workload manager. The user can request computational resources by uploading job scripts, and the system will manage the workload based on available resources and assign them to the user.

Table 2.3: Configuration of Delftblue

Node Category	Number	Cores	CPU/GPU	Memory	SSD
Standard	218	48	2x Intel XEON E5-6248R 24C 3.0 GHz	192 GB	480 GB
Fat type-a	6	48	2x Intel XEON E5-6248R 24C 3.0GHz	768 GB	480 GB
Fat type-b	4	48	2x Intel XEON E5-6248R 24C 3.0 GHz	1536 GB	480 GB
GPU	10	48	2x AMD EPYC 7402 24C 2.80 GHz 4x NVIDIA Tesla V100S 32 GB	256 GB	

The preparation of the simulation files is done on the local computer and the general workflow is presented in Figure 2.15. The first step is to prepare the rough surface models. The generation of the surface models is done by MATLAB, and the conversion and adjustment of the generated models is done by a Python script in Blender. In the second stage, simulation files are generated using FEKO. An initial simulation that contains all the simulation settings except the geometrical model is created. Then, the rough surface models are added to this initial simulation, and the model properties are set according to the instructions in Section 2.5.1 on one model. At last, the model is saved as a new simulation file. The automation of the FEKO operation can be achieved by using the FEKO API (Application Programming Interface), which allows the user to control operations using external scripts. Then the prepared simulation files are ready to be uploaded to DelftBlue.

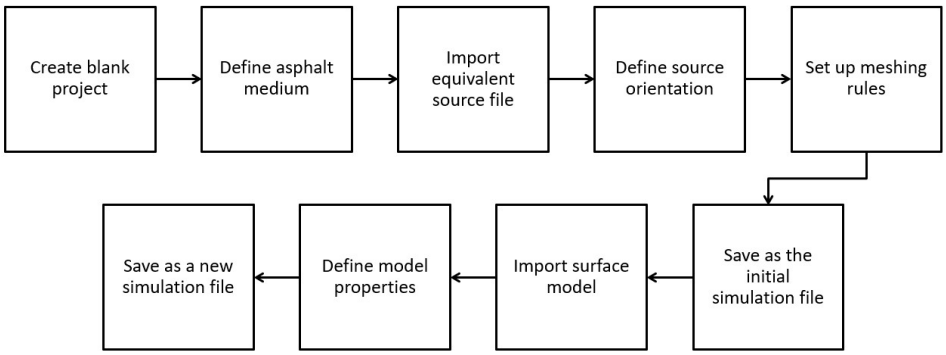

Figure 2.15: General workflow of setting up a simulation for Delftblue on the local computer

The FEKO kernel consists of several components, and the typical workflow of FEKO is described in Figure 2.16. For GUI, this workflow of the FEKO kernel is sequentially arranged and executed by selecting the Solve/Run tab. However, the operating system of DelftBlue does not have a GUI. Therefore, the FEKO components execution need to be executed via the command line [34]. Three commands were required to solve models on DelftBlue: cadfeko batch, prefeko, and runfeko. The first two commands create the mesh for the geometrical model from the cfx file and integrate the requested controls and outputs from the user, followed by the generation of a fek file that is ready for the FEKO solver to compute the requested outputs. The solver computes the outputs based on the fek file, which is the most computationally intensive task.

The workflow for setting up simulation jobs in Delftblue is explained in Figure 2.17. The Slurm queuing system organizes work according to its resource requirements, resulting in shorter waiting times for tasks that require fewer

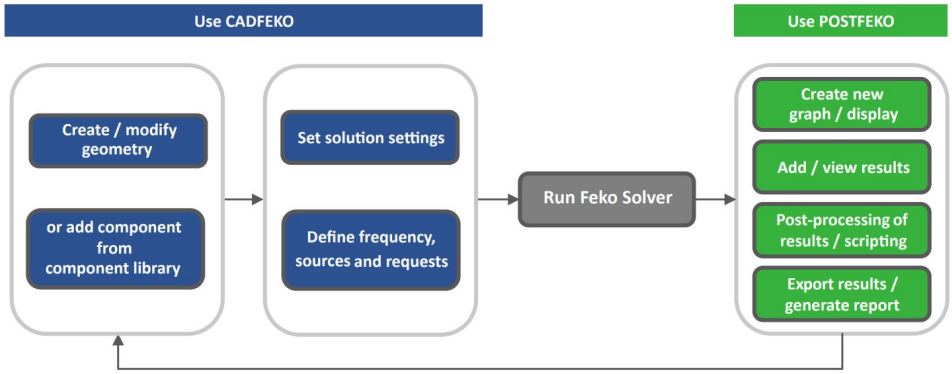

Figure 2.16: Typical workflow of FEKO components [34]

resources. To increase the efficiency of the simulation, the commands are executed in two job scripts and run on two types of nodes. The meshing of the model is executed on a standard compute node, while the solving is executed on a memory node with a 749 GB memory configuration. The result files are then transferred back to the local computer for further post-processing.

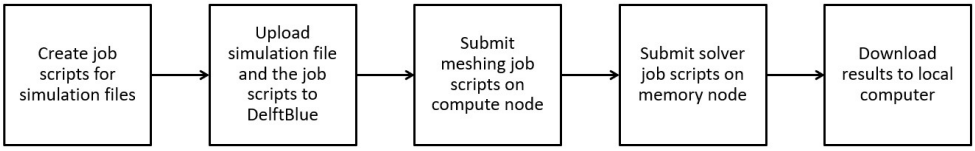

Figure 2.17: Workflow of setting up simulation jobs on Delftblue

2.6. Normalization of RCS

The post-processing of the results involves calculating the averaged far field and the normalized RCS. The first step of post-processing is to verify the accuracy of each result. The result may not converge when the maximum number of solver iterations is reached. In this instance, the solver quits and produces incorrect results. An example of an unconverged result and a converged result is shown in Figure 2.18. Those abnormal results need to be removed from the dataset before averaging the results. As the figure shows, the difference between these two results can be easily identified, and in the output log files, a warning message will also be reported if this solution is unconverged. The selection of the results can be done by viewing each far field result manually to find out whether or not it contains a solution warning.

The average result can then be calculated over the filtered result sets. The average gain is obtained by calculating the average gain of 30 realizations, the gain on each position in the far field is averaged individually, while the average RCS is obtained by calculating the RCS of each realization and then taking the average value of 30 realizations. For the calculation of the RCS, the RCS of a single brick model can be calculated from the far field result by:

$$\sigma_{Total} = 4\pi \frac{|E_{far,\theta}|^2 + |E_{far,\phi}|^2}{P_0} \tag{2.6}$$

$$\sigma_{Horizontal} = 4\pi \frac{|E_{far,\phi}|^2}{P_0} \tag{2.7}$$

$$\sigma_{Vertical} = 4\pi \frac{|E_{far,\theta}|^2}{P_0} \tag{2.8}$$

in which the $E_{far,\theta}$ and $E_{far,\phi}$ are the vertically and horizontally polarized components of the electrical field strength and P_0 is the incident power density [18]. The incident power density can be calculated in FEKO by placing an observation point at the surface center and requesting the electric and magnetic field strengths. The electric field strength at the observation point is $E_0 = 6.83137$ MV/m and the magnetic field strength is $H_0 = 18133.6$ A/m. The power density at the observation point can then be calculated by:

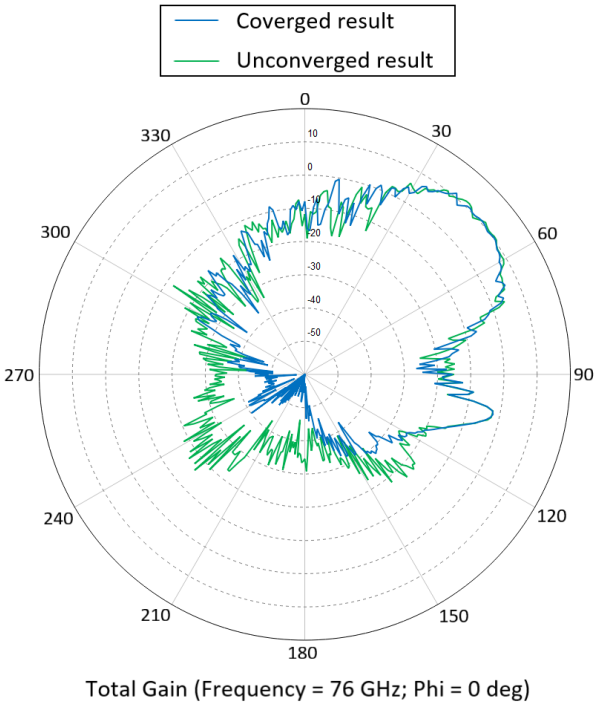

Figure 2.18: One of the converged far field results and an unconverged result

$$P_0 = \frac{1}{2} |E_0| \cdot |H_0| = 61950 \; MW/m^2 \tag{2.9}$$

According to the radar equation, the incident power density can also be calculated by:

$$P_0 = \frac{P_t G_t}{4\pi R^2} \tag{2.10}$$

in which P_t is the total radiated power by the source and G_t is the gain of the source. The values of these variables can be found in the output file. R is the range between the source and the incident point with $R = 100\sqrt{2}$ mm. The resulting incident power density $P_0 = 64504.7$ MW/m^2, which is close to the simulated value.

The normalized RCS of the surface can be computed by:

$$\sigma_0 = \frac{RCS_{Total}}{S} \tag{2.11}$$

where RCS_{Total} represents the total RCS of the entire surface, and S is the size of the radar-illuminated area on the surface. In this case, the total RCS is the average RCS result of 30 realizations. To compute this, the size of the illuminated area is required, which can be calculated by the radar range equation. The received power can be calculated as follows:

$$P_r = \frac{P_t G_t G_r \lambda^2}{(4\pi)^3 R^4} \tag{2.12}$$

The antenna footprint is then taken as the antenna radiates on the surface plane area with normalized received power larger than -10 dB. Figure 2.19 shows the x-y plane projection of the antenna footprint with 45° incident angle.

As shown in the figure, the shape of the footprint is an ellipse-like shape and the received power is not uniformly distributed over this area. Most of the received power is located in the center of the ellipse. Therefore, a two-dimensional Gaussian window is applied for weighting to calculate the illuminated area, as shown in Figure 2.20. For the source placed at an incident angle of 45°, the illuminated area size is about 0.0094 m^2.

Following the procedure above, Table 2.4 presents the illuminated area size at different incident angles. These values can be used to compute the normalized RCS of different surfaces in the following chapters.

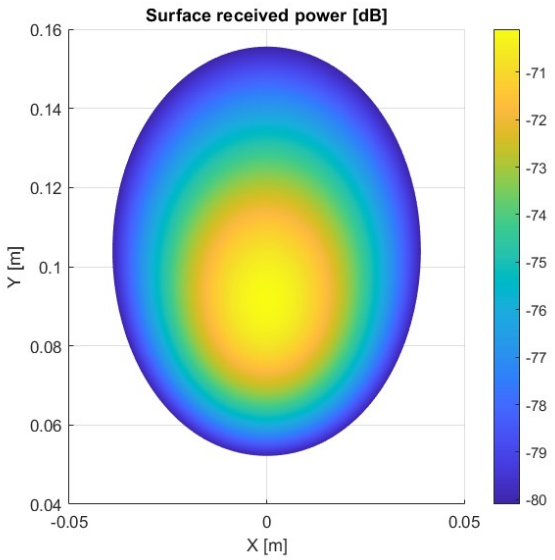

Figure 2.19: The antenna footprint based on the normalized received power

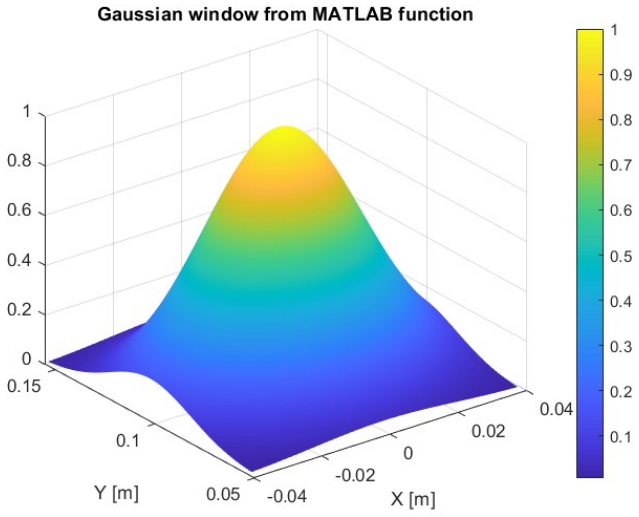

Figure 2.20: 2D Gaussian window

Table 2.4: Illuminated area size for four polarization components at different incident angles

	HH(m^2)	HV(m^2)	VH(m^2)	VV(m^2)
37.5°	0.0085	0.0088	0.0088	0.0086
45°	0.0094	0.0094	0.0094	0.0093
52.5°	0.0104	0.0105	0.0105	0.0104
60°	0.0119	0.0117	0.0117	0.0116

2.7. Limitations

Due to the limitations of the available computational resources, the simulation model has a number of limitations. Figure 2.21 presents the surface current distribution at an incident angle of 60°. The current level on the left edge of the surface is approximately 9 dBA/m, while on the right edge, it is approximately 54 dBA/m. The strength of the current indicates that the right part of the surface is excited, causing diffraction. To suppress the diffraction level, the current on the right side of the edge must be reduced to less than 9 dBA/m as well.

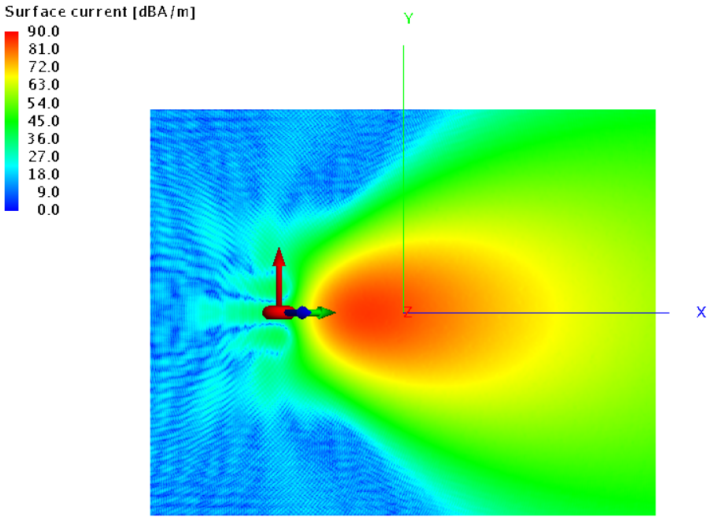

Figure 2.21: Surface current distribution of surface with RMS height of 0.02 mm and correlation length of 2 mm and incident angle of 60°

Specular scattering contributes the most to the scattered field for a flat surface, while diffraction is responsible for the backscattered power. Figure 2.22 shows the far field of the scattered field of a flat surface with an incident angle of 60°. The backscattering lobes around $\theta = 240°$ and $\theta = 300°$ are the results of diffraction. The diffraction is independent of surface roughness and is positioned in the direction of backscattering that interferes with the RCS result in the case of a rough surface. If the backscattered power from the rough surfaces is comparable to or less than the diffraction strength, then the RCS result for this model becomes less accurate.

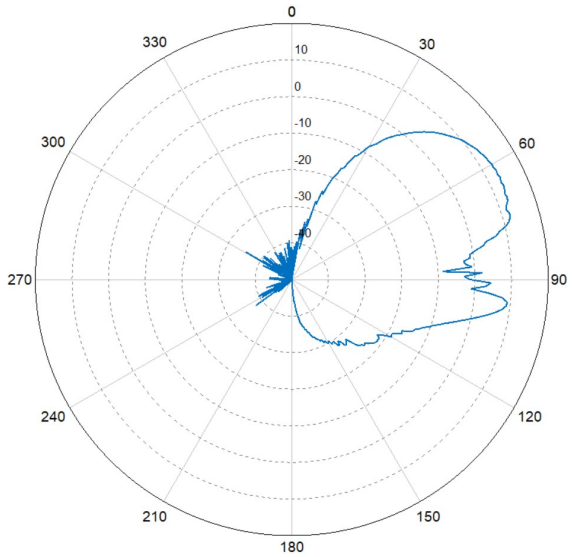

Figure 2.22: Far field pattern at $\phi = 0°$ of the flat surface with an incident angle of 60°

The second issue is the limited size of the source footprint. The scattered field curve for the rough surface consists of multiple peaks, and the position of these peaks depends on the height distribution and the surface size. As a result, for the random surfaces, the position of the peaks is randomly distributed. When performing the averaging for a set of rough surface results, these peaks from different results will interfere with one another, causing the result to be inaccurate. Figure 2.23 shows the difference between the scattered fields of different sizes of the footprint. The simulation is done on the original size of the rough surface and a rescaled surface, which is created by taking half of the original size of the surface from the center. The footprint size on the rescaled surface is the same as the original surface. The results show that for a relatively smaller footprint, the variation of the peaks is larger. Therefore, the peaks can be suppressed by a larger footprint or a larger number of results. However, to suppress the diffraction, a larger footprint would require a larger surface size as well.

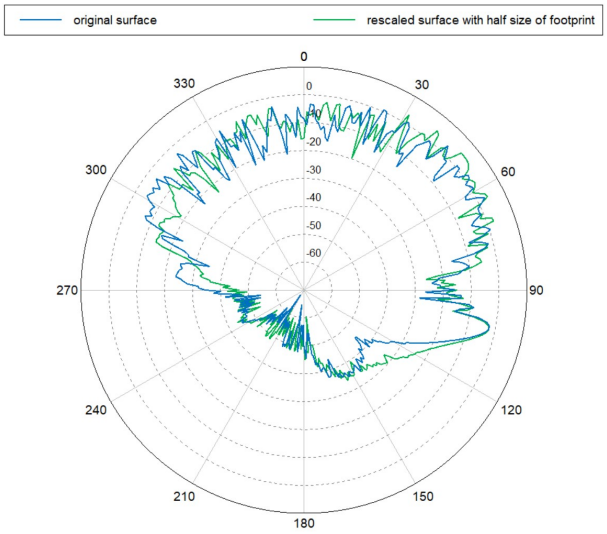

Figure 2.23: Comparison of the far field at $\phi = 0$ of the original surface and surface with equivalent half size of footprint

The third issue is the beam width of the source. The incident power is shown in Figure 2.24, and the half-power beam width is 14 wavelengths. In other similar studies of scattering problems, the incident beam width is mostly around one wavelength, which is less than it is in this project [29][30][36]. Considering that the surface is located between the near field and the far field region of the source, the incident wave is a spherical wave. A large incident beam width results in a large phase difference in the surface current, which influences the calculation of the scattered field.

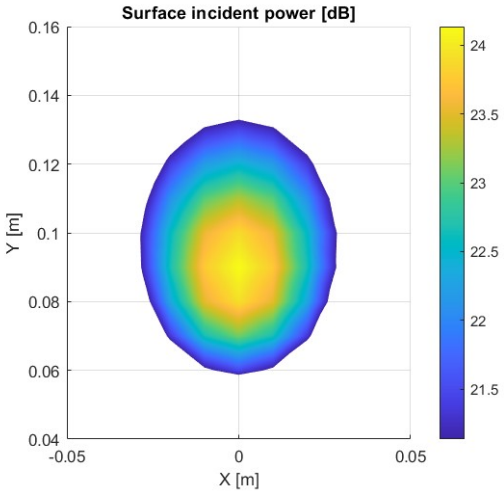

Figure 2.24: Incident power of dipole array source

The last issue is the orientation error of the source. The vertical source is obtained by rotating the horizontal source without adjusting the location. Ideally, the location of the source footprint for two polarization cases would be identical. However, the source incident point on the surface shifts toward the -x direction in the case of the vertical source compared with the case of the horizontal source. This shift is the consequence of the asymmetry of the source radiation, the footprint location shifts for the vertical case, resulting in incoherent results for the two polarization cases.

2.8. Conclusion

In this chapter, the development of the computational model is explained. The procedure for developing the model includes the generation of the synthetic surfaces, the selection of the surface's size and source, the parameter selection of the simulation, and the number of Monte Carlo method realizations. After the model has been designed, it is simulated on the MS3 server and the DelftBlue supercomputer. The post-processing of the simulation results is also explained, in which the calculation of the averaged far field RCS of the surface is explained. The simulations are successful on both the MS3 server and Delftblue. and the simulation results are obtained. The post-processing procedure is used in the later chapters to present the results.

Examining the simulation outcomes revealed that the developed model has limitations. However, extending the limits requires more computational resources, which are beyond the scope of this project. As a result, the model designed for this project has some limitations on the accuracy of challenging cases of combinations of surface and source parameters.

3

Numerical analysis of dielectric surface

In this chapter, the results of the developed numerical model are presented and explained. Different parameters that influence asphalt scattering are investigated. The scattering properties are evaluated in terms of the averaged far field gain, the BSC, and the RCS dependency of the surface parameters. In Section 3.1, the scattering of surfaces with different roughnesses is studied, and in Section 3.2, the scattering at different incident angles for the rough surface is studied.

3.1. RMS height

The roughness of the surface can be characterized by its RMS height and correlation length. In this section, the average far field result, the BSC, and the RCS of the rough asphalt surface with different RMS heights are presented.

The incident angle is 45° and surfaces with the same correlation length of 2 mm and three different cases of different RMS heights are compared, which are 2 mm, 0.2 mm, and 0.02 mm. The horizontally and vertically polarized sources are simulated individually. In addition to the comparison, a fourth case of a flat asphalt surface is simulated in the same conditions. The detailed simulation settings are shown in Table 3.1:

Table 3.1: Simulation setting for different RMS heights

Parameters	**Setting**
Surface size	500*400*80 mm
Medium	asphalt
Incident angle	45°
Source polarization	horizontal (H), vertical (V)
Source distance d	$100\sqrt{2}$ mm
Correlation length (l)	2 mm
RMS height (σ)	case 1: 2 mm case2: 0.2 mm case 3: 0.02 mm

An example of the 3D view of the far field result for a simulation of case 1 is shown in Figure 3.1. The figure shows the orientation of the Cartesian coordinates of the model. The source is incident at $x = -100$ mm, $y = 0$ mm, and $z = 100$ mm, with a rotation of 45°. In the corresponding spherical coordinate system, the source is located at $\theta = 315°, \phi = 0°$.

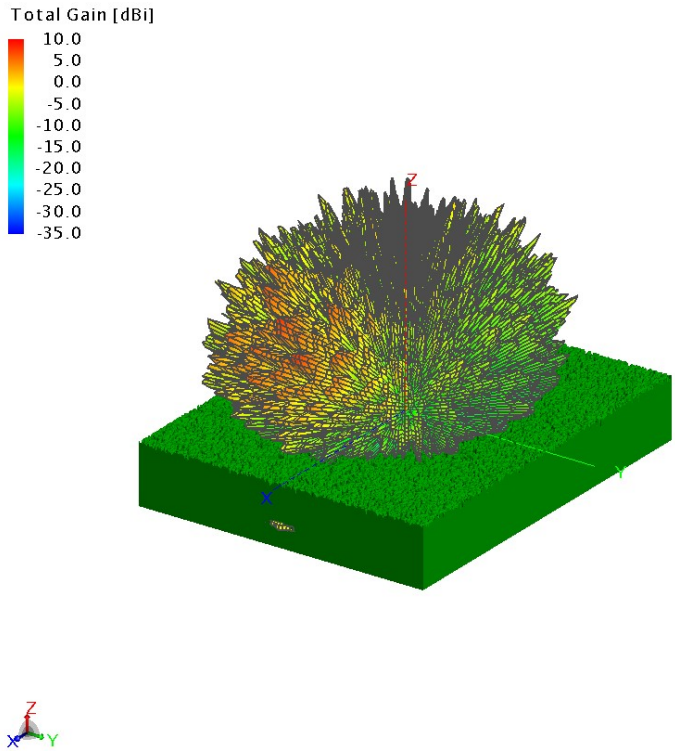

Figure 3.1: An example of the far field result

Taking the ϕ-cut at $\phi = 0°$, the average far fields for rough surfaces and the far field of the flat surface with two kinds of polarization are shown in Figure 3.2 and 3.3. As presented in the figures, at forward scattering, a main lobe can be observed at $\theta = 45°$. For backscattering, the diffuse scattering becomes stronger as the RMS height increases, independent of source polarization. For rougher surfaces, the scattered power is more evenly distributed on the upper bounds of the surface, with more power being distributed in the backscattering direction than in the smoother surface case.

In the case of a horizontally polarized source, the main lobe of forward scattering can be observed at 45° in all cases except case 1. The forward scattered power is decreased by 10 dB for case 1 compared to the other cases. For backscattering, at $\theta = 315°$, the backscattered power for case 1 is the largest due to diffuse scattering and it is increased by 40 dB from case 4 to case 1.

In the case of a vertically polarized source, the Brewster angle is given by:

$$\theta_B = arctan(\sqrt{\frac{\epsilon_r}{\epsilon_0}})$$

where the ϵ_r is the dielectric constant of the asphalt and ϵ_0 is the dielectric constant of the free space. In this case, the Brewster angle is 63° and it can be easily observed for all cases except case 1. The forward scattered power for case 1 is decreased by 15 dB compared to the other cases. The backscattered power for case 1 is increased by 40 dB from case 4 to case 1.

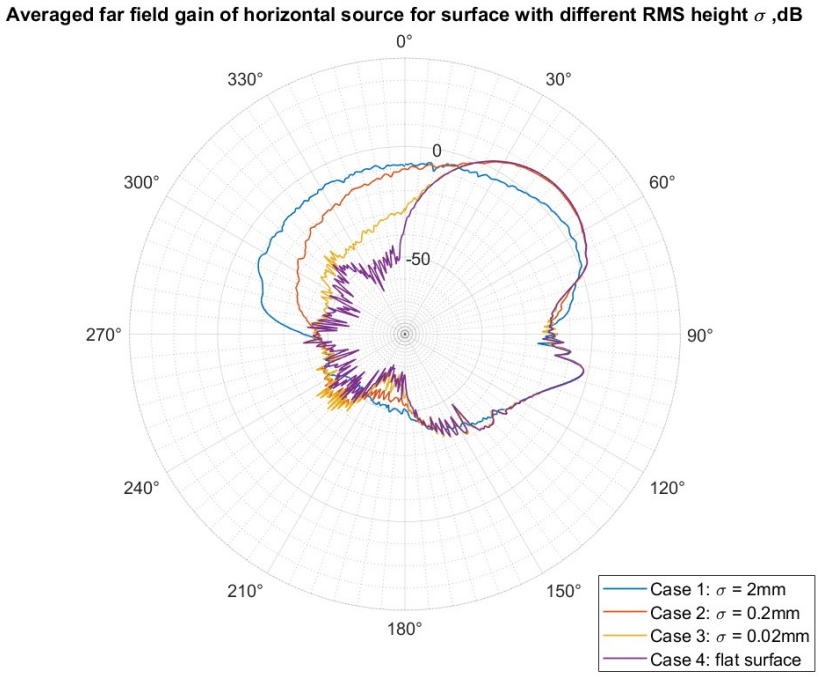

Figure 3.2: Average far field results of different RMS heights with a horizontally polarized source

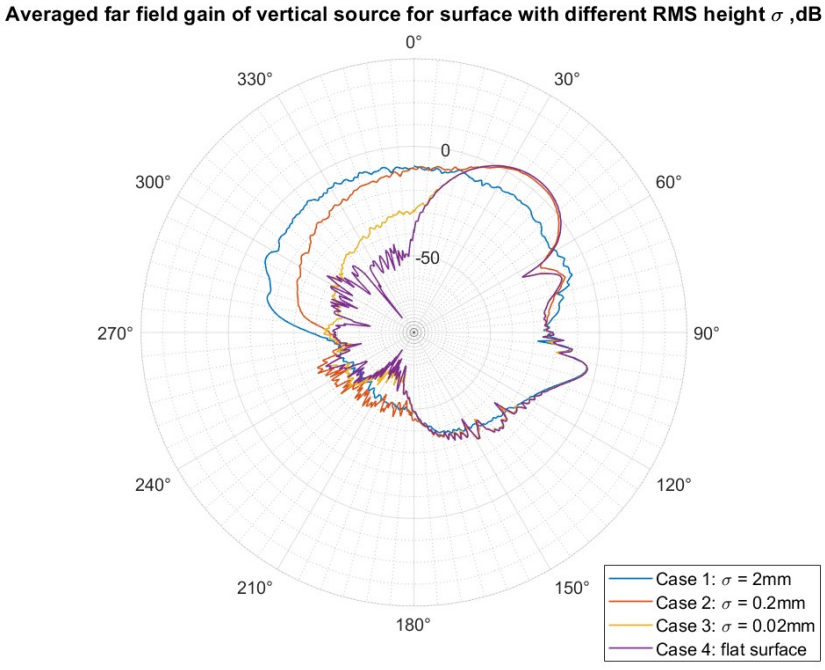

Figure 3.3: Average far field results of different RMS heights with a vertically polarized source

Figure 3.4 shows the normalized BSC of the four polarization components (HH, HV, VH, and VV) for four cases. In general, the cross-polarized components of cases with a rough surface are larger than those with a flat surface and grow as the RMS height increases in all directions. The co-polarized components only increase in the backward direction. The difference in BSC for backscattering between case 1 and case 4 is 40 dB for co-polarized components and 50 dB for cross-polarized components.

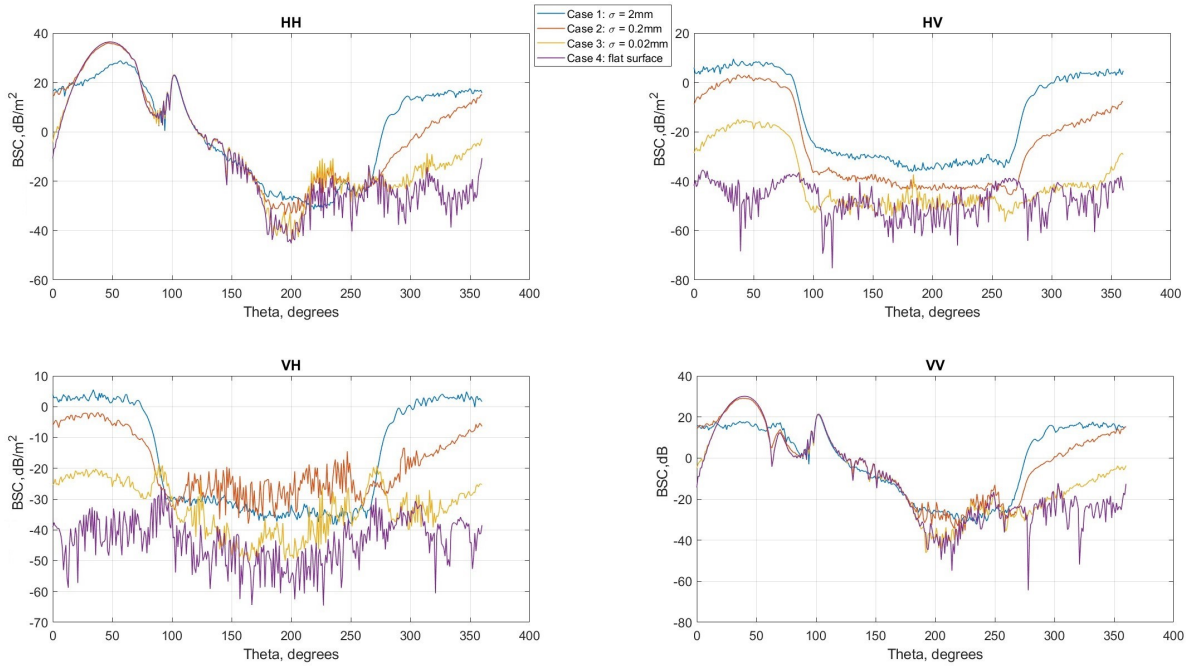

Figure 3.4: Normalized BCS dependency with different RMS heights

Taking the BSC value at $\theta = 315°$, the RCS dependence of surface RMS height is presented in Figure 3.5. The error bar represents the standard error of the result set. The normalized surface RCS increases with the RMS height. The vertical components are generally larger than the horizontal components, except for surfaces with $\sigma = 0.02$ mm. For the case of $\sigma = 0.02$ mm, the HH component is larger than the HV component by 30 dB, and the VV component is larger than the VH by 10 dB. In addition, the difference between the HH and VV component is 3 dB whereas the difference between the HV and VH is 12 dB. As the RMS height increases, the differences between the horizontal and vertical components reduce. For $\sigma = 2$ mm, the difference between the HH and VV, HV and VH is negligible, and the difference between the co- and cross- polarization components is reduced to 15 dB. From the case of $\sigma = 0.02$ mm to $\sigma = 2$ mm, the co-polarized components HH and VV are increased by 34 dB, the VH component is increased by 43 dB, and the HV component is increased by 30 dB.

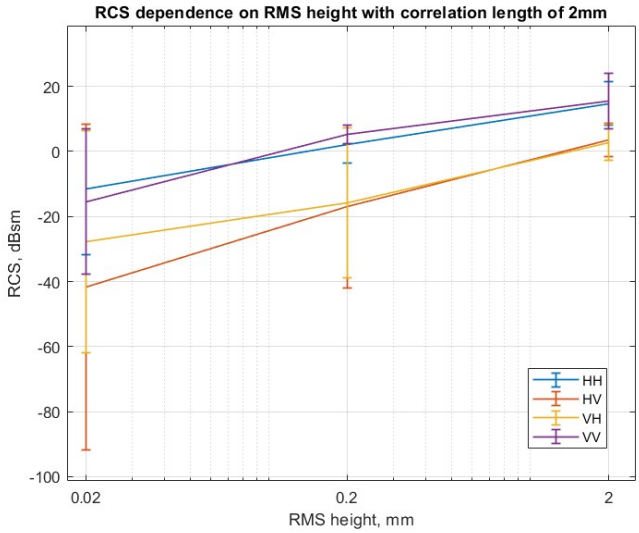

Figure 3.5: RMS height dependence of RCS with 45° incident angle

3.2. Incident angle

In this section, the results of the scattering from different incident angles are presented and explained. The incident angle of the simulation increases from 37.5° to 60° with a 7.5° step. The simulated surfaces are the same for all the incident angles with RMS height $\sigma = 2$ mm and correlation length $l = 2$ mm. The horizontally and vertically polarized sources are simulated individually. The detailed simulation settings are shown in Table 3.2:

Table 3.2: Simulation setting for different incident angles

Parameters	Setting
Surface size	500*400*80 mm
Medium	asphalt
Incident angle	37.5°-60°
Source polarization	horizontal, vertical
Source distance (d)	$100\sqrt{2}$ mm
Correlation length (l)	2 mm
RMS height (σ)	2 mm

The orientation of the coordinates and the sources are the same as shown in Figure 3.1, in the corresponding spherical coordinate the incident angle ranges from 300° to 322.5°. The averaged far fields of different incident angles with two kinds of source polarization are shown in Figure 3.6 and Figure 3.7. The direction of the diffraction lobe shifts along the incident angle, as shown by the figures, whereas the backscattered power is not substantially affected by the incident angle.

The BSC of four components with different incident angles is shown in Figure 3.8. The normalized BCS are close to each other for different incident angles, except in the direction of the diffraction lobe. For a smaller incident angle, the BCS in the direction of backscattering is slightly larger.

The RCS dependence of the incident angle is presented in Figure 3.9. The normalized RCS decreases as the incident angle increases. The value for four RCS components at 60° is 3 dB for co-polar components and 7 dB for cross-polar components, which is less than their value at an incident angle of 37.5°. The HH and VV values, as well as the HV and VH values, are close to each other in all angles, except for the incident angle of $\theta = 60°$, where the difference between the HH and VV is 3 dB. Generally, the co-polarized components are larger than the cross-polarized components by 10 dB.

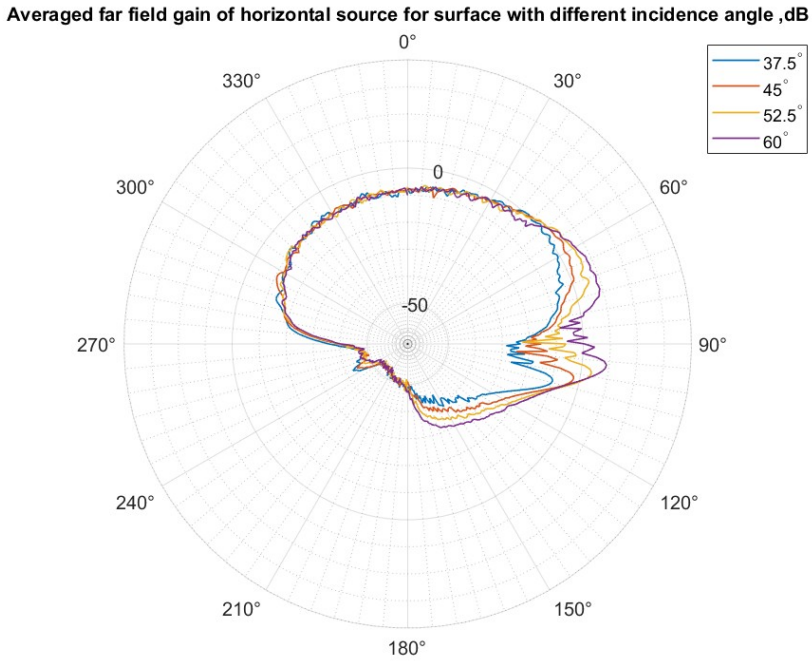

Figure 3.6: Average far field results of different incident angles with a horizontally polarized source

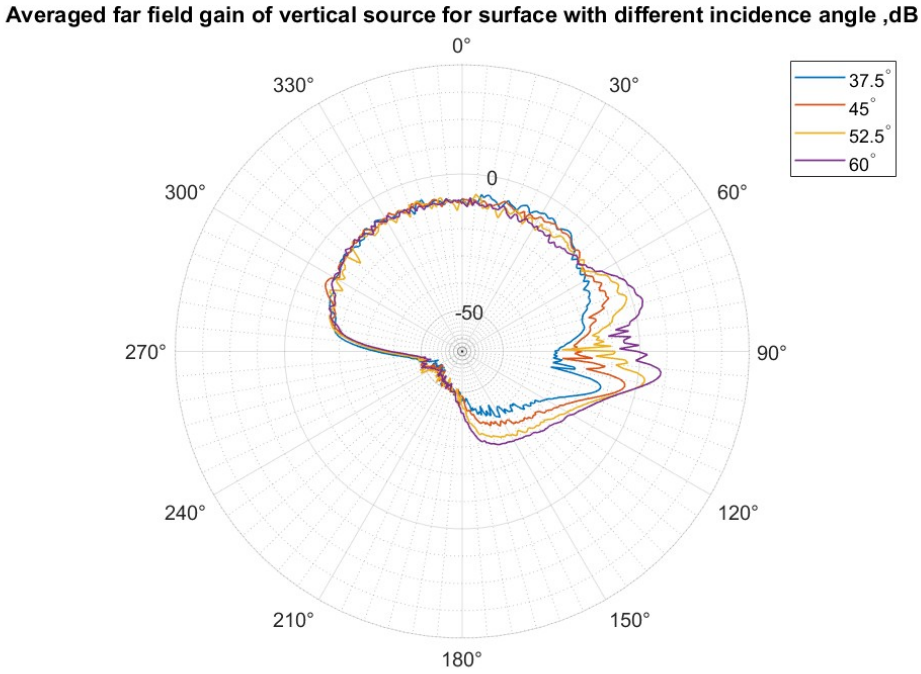

Figure 3.7: Average far field results of different incident angles with a vertically polarized source

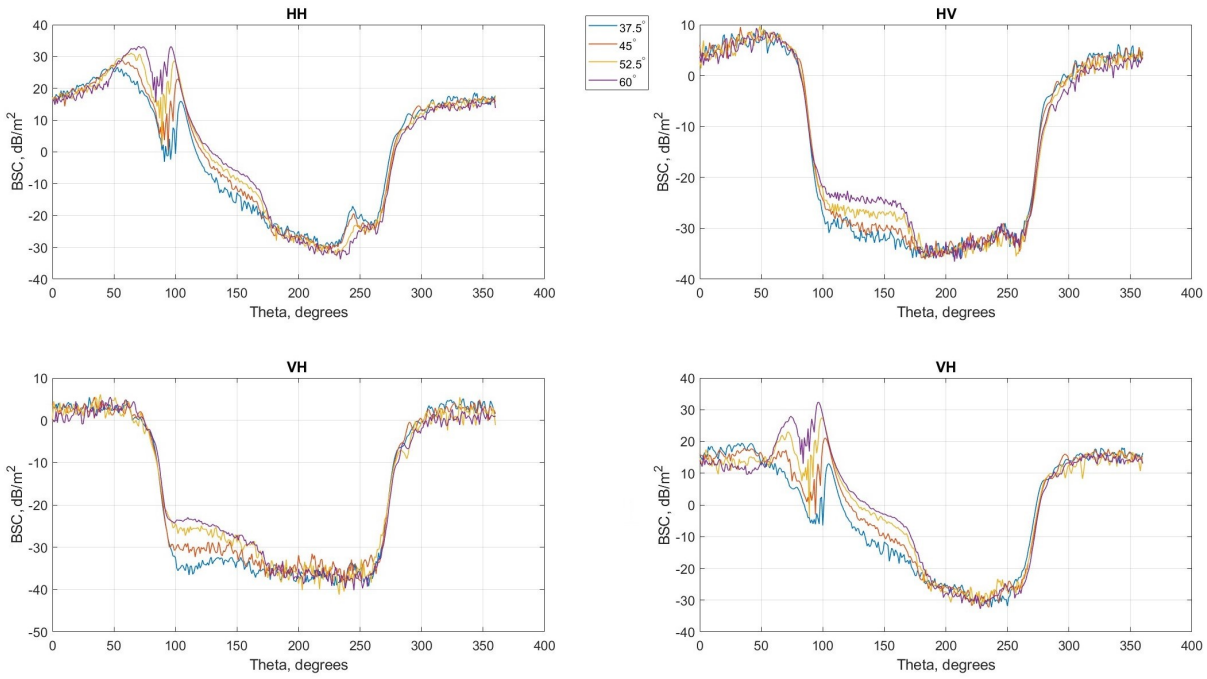

Figure 3.8: Normalized BCS dependency with different incident angle

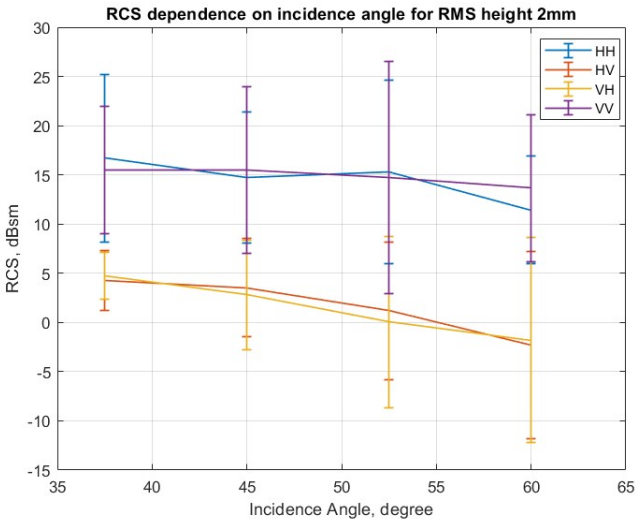

Figure 3.9: Incident angle dependence of RCS

3.3. Conclusion

In this chapter, the results of the numerical model are presented and explained. This includes the results of surfaces with different RMS heights and different incident angles. For surfaces with a larger RMS height, the surface is rougher and more power is scattered backward. The cross-polar components of the BSC increase compared to the flat surface when the surface becomes rougher. Compared to a surface with an RMS height of 0.02 mm, the RCS value of a surface with an RMS height of 2 mm increased by 30 to 40 dB. When the surface is extremely rough, the difference between the horizontal and vertical components decreases and becomes negligible. For the study of different incident angles, the RCS decreases as the incident angle increases. From the incident angle of 37.5° to 60°, the four components of RCS decrease by about 3 dB to 7 dB.

These results show that there is not much difference in the RCS between the two polarizations when the surface is very rough. Generally, the difference between the co-polar and cross-polar components is larger than 10 dB for all the rough surface cases. A larger RMS height and smaller incident angle result in a smaller RCS of the surface.

4

Numerical analysis from multi-layered surface

In this chapter, the model of the multilayer surface and the simulation results of the model are presented and explained. The development of the multilayer model starts with the design of the model and then moves to the realization of the model in FEKO, this procedure is explained in Section 4.1. After the model is developed, a small number of simulations are executed to obtain insight into the scattering of the multilayered surface. The simulation parameters are presented in Section 4.2 and the results are presented in Section 4.3.

4.1. Multi-layered surface model

To investigate the impact of the additional layer on the asphalt, a two-layer model is designed. In particular, the effect of an additional water layer is investigated. The model is composed of an asphalt layer and a water layer on top of the asphalt layer. Figure 4.1 is an example of the two components of the model in Blender. As shown in this figure, on top is the water layer, and beneath it is the asphalt layer. To eliminate the air gap between layers, the bottom surface of the water layer is precisely matched to the top surface of the asphalt layer. The upper surface of the water layer is flat, simulating the situation in which the road is completely covered by still water. The thickness of the water layer is larger than the highest point of the asphalt surface to make sure that the asphalt layer is fully covered.

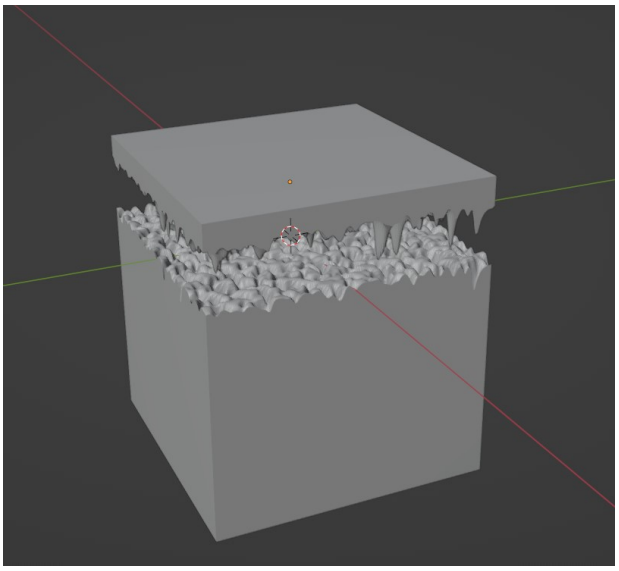

Figure 4.1: An example of the two-layer model

In FEKO, these components are imported individually and need to be merged into one model. An overview of the workflow for setting up a multilayered model on the MS3 server is shown in Figure 4.2.

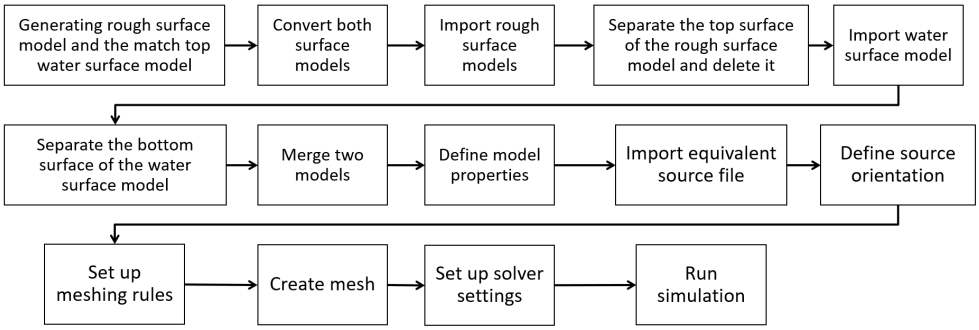

Figure 4.2: Workflow of creating multilayer models in FEKO

Due to the import process, the coincident surfaces of the two layers will be recognized as overlapping meshes and cause meshing errors. To resolve such errors, the imported model surface is regrouped, and the coincident surfaces are separated from the other part of the model. The coincident surface of the asphalt layer is then deleted. This makes the asphalt layer an open surface model, which FEKO warned could lead to calculation errors. Therefore, two layers must be merged into a closed surface model. This can be done by using the merge mesh option. On the mesh setting tab, the front medium of the water layer is set to free space, while the back medium is water. Similarly, the front medium of the asphalt layer is set to free space, while the rear medium is asphalt. The front medium of the interface is set to asphalt and the back medium is water. The rest of the steps of model construction are the same as for single-layered models. The finished model is presented in Figure 4.3.

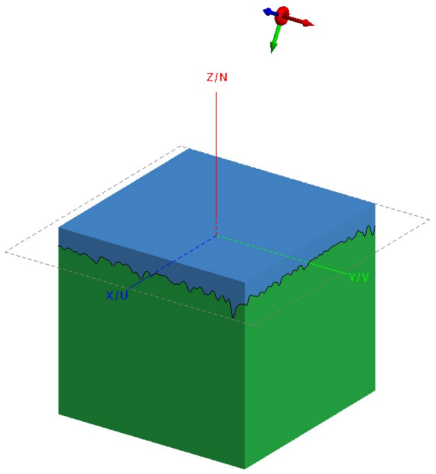

Figure 4.3: Two-layer model in Feko

4.2. Simulation on a piece of the two-layer model

After the model is ready, a trial simulation is done on the MS3 server. The size of the surface is decided to be 140 mm * 140 mm taking into account the computer configuration. The thickness of the asphalt is 80 mm and the thickness of the water layer is 10 mm. The relative permittivity of the asphalt is the same as in the previous simulations, and the relative permittivity of the water is $\epsilon_{water} = 5.6 - j1.7$ [7]. The corresponding conductivity of the water is 7.42 S/m at 76 GHz according to Equation 2.5.

To keep the radar footprint within the surface of this size, the source is placed at 30° with a distance to the surface $d = 130$ mm.

4.3. Numerical results from multi-layered surface

After succeeding in a trial simulation, the investigation then expands to a batch simulation. The detailed simulation settings are shown in Table 4.1.

Table 4.1: Simulation setting for two-layer model

Parameters	Setting
Surface size	140*140*80 mm for asphalt 140*140*10mm for water
Medium	asphalt, water
Incident angle	30°
Source polarization	horizontal, vertical
Source distance	130 mm
Correlation length	2 mm
RMS height	2 mm

An example of the far field pattern with a horizontal source is presented in Figure 4.4. The blue line indicates the boundary of the model. Taking $\phi = 0$, the average far field for the two-layered surface in two kinds of polarization is shown in Figure 4.5. The backscattered power for two polarizations is comparable. Theoretically, the Brewster angle for the asphalt layer is $\theta_{B1} = 63°$, whereas the Brewster angle for the water layer is $\theta_{B2} = arctan(\sqrt{\frac{\epsilon_{water}}{\epsilon_0}}) = 67°$. According to the vertical source's output, the Brewster angle is 70 degrees.

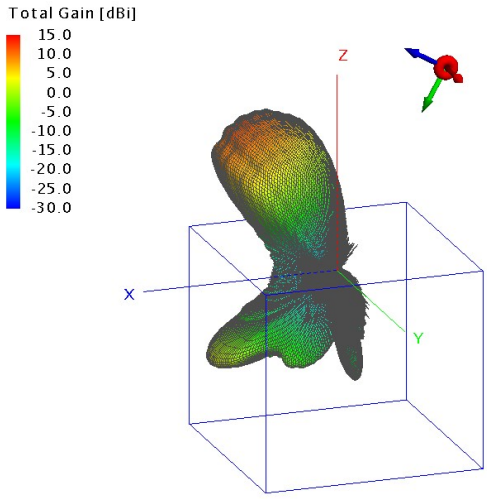

Figure 4.4: Example of the far field result for the two-layer model with a horizontally polarized source

A comparison between the single layer of the asphalt surface and the two-layer surface is shown in Figure 4.6 and 4.7. Since the air void of the asphalt surface is filled by water, the top surface becomes a smooth, flat surface. Consequently, the specular scattering becomes stronger. In comparison to the asphalt surface, the two-layered model reduces the backscattering power by 25 dB for horizontally polarized sources and 20 dB for vertically polarized sources. On the other hand, for forward scattering, the forward scattered power increases by 10 dB compared with the flat surface case for both polarized sources.

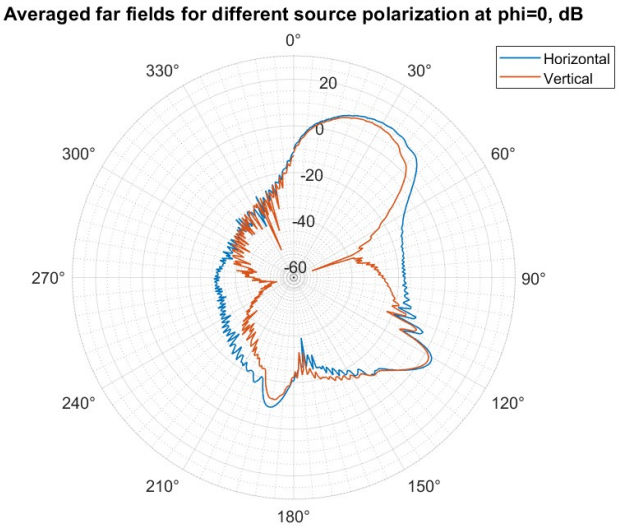

Figure 4.5: Average far field for the two-layered model

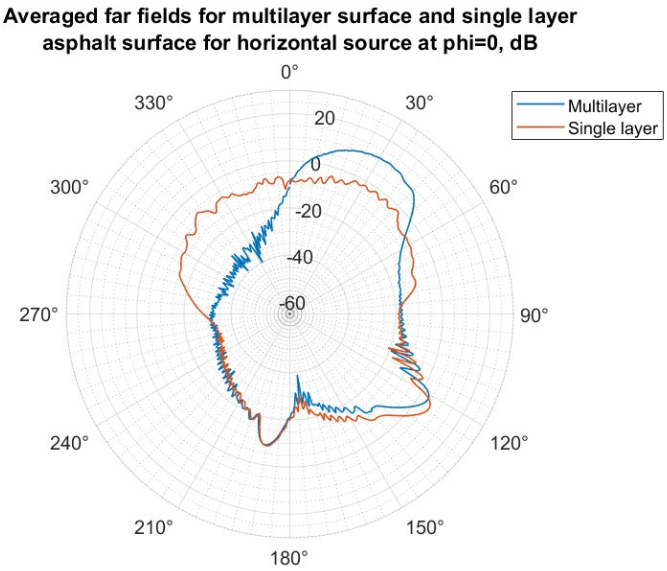

Figure 4.6: Average far field for the two-layered model and the single-layer model with a horizontally polarized source at 30°

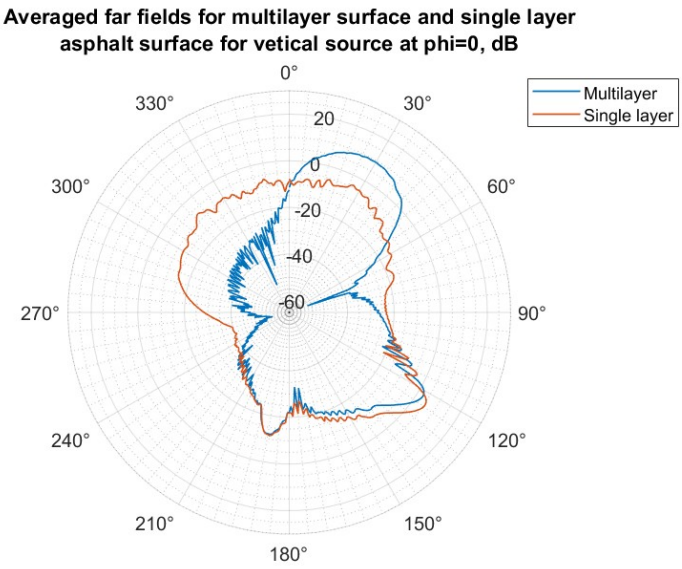

Figure 4.7: Average far field for the two-layered model and the single-layer model with a vertically polarized source at 30°

4.4. Conclusion

In this chapter, based on the single-layer model, a two-layered model is designed to study the impact of an additional water layer on the scattering properties. Similar to the single-layer case, the model is constructed in FEKO by adding a water layer to the asphalt surface. The configuration of the simulation of the multi-layer model is determined by the available computational resources. The simulation results show that an additional flat water layer results in stronger specular scattering, resulting in a 20 to 25 dB decrease in the backscattered power and an increase in 10 dB of the forward scattered power.

5

Verification

In this chapter, the verification of the model is explained. The numerical model is validated by comparing the simulation outcome to the SPM theory. SPM is an analytical model that can be applied to slightly rough surfaces and the details of this model are discussed in Section 5.1. The comparison of the designed model and SPM are shown in Section 5.1.1 and 5.1.2. In the case of a surface with a small RMS height, the correlation length can be varied while remaining within the validation region of SPM. The verification consists of two parts: the first is the surface with small correlation lengths, and the second is the surface with a large correlation length.

5.1. Theoretical verification

As explained in Section 1.2, SPM provides reliable predictions for slightly rough surfaces, and it has been used for model validations in many cases [37]. The validation region of the SPM for the surface properties is that the surface should be relatively small in RMS height and slope, which can be expressed by:

$$(k_z\sigma)^2 \ll 1 \tag{5.1}$$

$$\frac{\sigma}{l} \ll 1 \tag{5.2}$$

where:

k_z: the vertical component of the wave vector.

σ: surface RMS height.

l: surface correlation length.

According to SPM, the backscatter coefficients of a single-layered rough surface can be calculated by [37]:

$$\sigma_v = \frac{4k_0^4|\epsilon-1|^2\cos^4\theta\hat{B}(-2\vec{k})|\epsilon\sin^2\theta+(\epsilon-\sin^2\theta)|^2}{|\epsilon\cos\theta+(\epsilon-\sin^2\theta)^{1/2}|^4} \tag{5.3}$$

$$\sigma_h = \frac{4k_0^4|\epsilon-1|^2\cos^4\theta\hat{B}(-2\vec{k})}{|\cos\theta+(\epsilon-\sin^2\theta)^{1/2}|^4} \tag{5.4}$$

where:

k_0: the wavenumber in free space.

ϵ: the dielectric constant of the medium.

θ: the incident angle in spherical coordinates.

$\vec{k}$: the incident vector, $\vec{k} = k_0 \sin\theta\vec{x_0}$.

$\hat{B}(\vec{k})$: the spectrum of the surface correlation function, with $B(r) = \int B(r)\exp(ik\cdot r)dr$

For a surface with a Gaussian correlation function, the expression of its correlation function is

$$B(x,y) = \sigma^2\exp\left[-(\frac{\sqrt{x^2+y^2}}{l})^2\right] \tag{5.5}$$

and the spectrum of the surface with Gaussian correlation function is given by:

$$\hat{B} = 4\pi^3\sigma^2 l_x l_y \exp\left(-2l_x^2 k^2 \sin^2\theta\right) \tag{5.6}$$

where l_x and l_y are the correlation lengths along the X and Y direction respectively.

5.1.1. Validation of surface with small correlation length and slope

The SPM has been used for the validation of numerical models of surfaces with relatively small correlation lengths and slopes. The surface parameters from Chen's research are used as a reference to design a set of surface parameters for the validation of the numerical model in this project [37]. The designed surface parameters are listed in Table 5.1.

Table 5.1: Surface parameters for model validation in the case of small correlation length and small slope

	RMS height (σ)	Correlation length (l)
Case 1	0.25 mm	0.4 mm
Case 2	0.2 mm	0.4 mm
Case 3	0.02 mm	0.4 mm

The SPM predictions of the horizontal backscatter coefficient for the three cases are shown in Figure 5.1. With the same correlation length, the slope of the backscattering coefficients for the three cases is the same, except the value is different due to the difference in RMS height. In the range of incident angles from 37.5° to 60 °, the horizontal backscatter coefficient decreased by 6.7 dB.

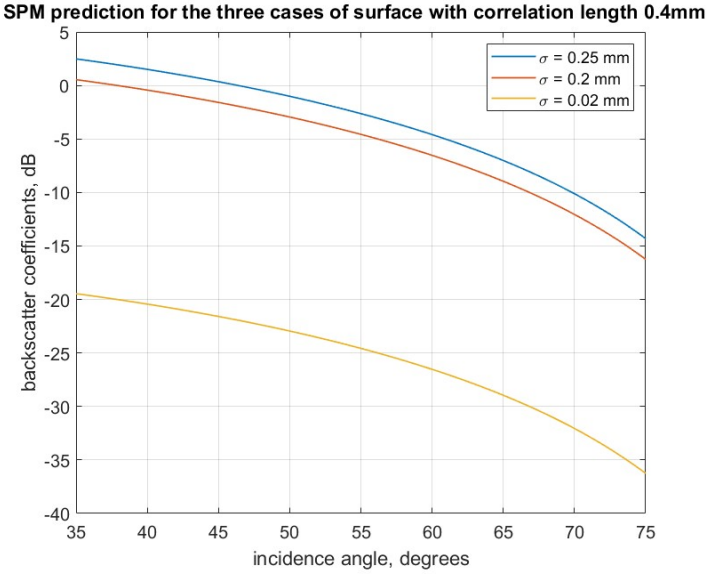

Figure 5.1: SPM prediction of the horizontal backscatter coefficient of the three cases of surface $l = 0.4$ mm

According to Section 2.4.3, the average result starts to converge with 10 realizations, resulting in a good accuracy of the results. Therefore, ten surfaces with horizontally polarized sources are simulated for validation. Figure 5.2, 5.3 and 5.4 present the comparison of the RCS obtained by the simulation and the theoretical results for three cases of RMS height, with both values are normalized with respect to the largest absolute value in the range. For surfaces with relatively small correlation lengths and slopes, the numerical model is generally consistent with the analytical model prediction with an error of 3 dB. The error could be caused by the computational error in the model calculation and the diffraction effects from the model.

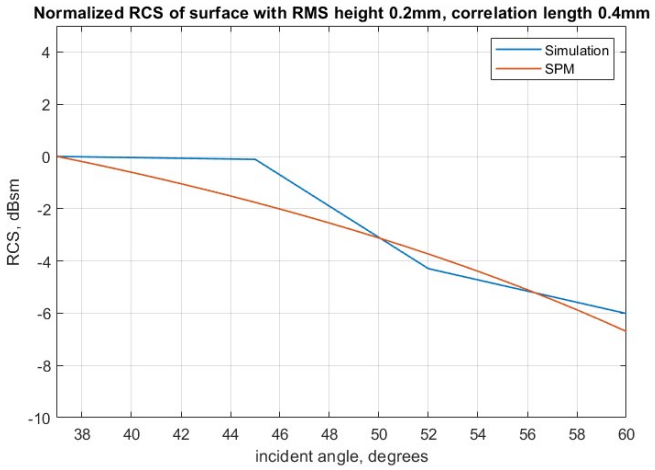

Figure 5.2: Comparison of RCS and SPM prediction for $\sigma = 0.2$ mm and $l = 0.4$ mm with horizontally polarized incident source

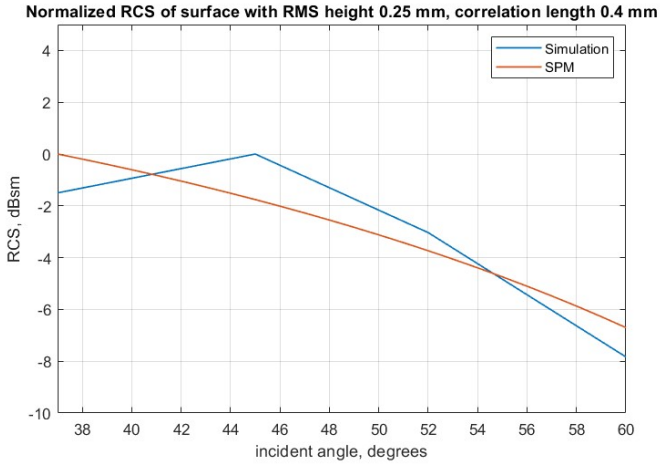

Figure 5.3: Comparison of RCS and SPM prediction for $\sigma = 0.25$ mm and $l = 0.4$ mm with horizontally polarized incident source

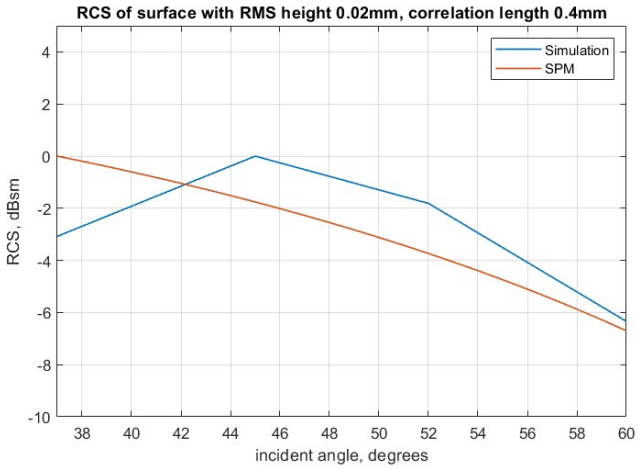

Figure 5.4: Comparison of RCS and SPM prediction for $\sigma = 0.02$ mm and $l = 0.4$ mm with horizontally polarized incident source

Figure 5.5 shows the comparison of the averaged scattered field and the flat surface case. In the case of a flat surface, scattering should only consist of specular scattering. As a result, the incident power will not be scattered backward by the surface. The backscattered power in the flat surface case is the result of edge diffraction. It is found that the backscattered power of the rough surface cases is larger than that of the flat surface case, indicating that the backscattering is not affected much by edge diffraction.

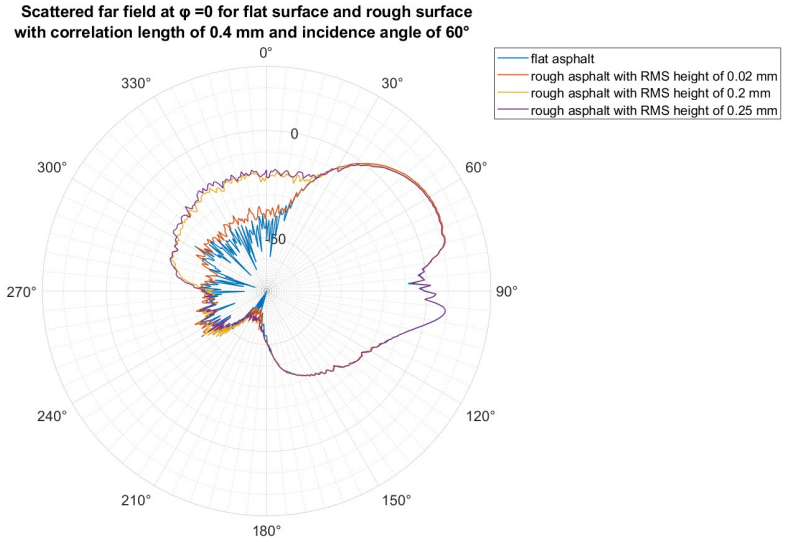

Figure 5.5: Far field at $\phi = 0$ with horizontal source incident at 60° between the three rough and the flat surface cases

5.1.2. Validation of surface with large correlation length and small slope

For surfaces with larger correlation lengths, the results of surfaces with an RMS height of 0.02 mm and a correlation length of 2 mm from Section 3.1 are compared with the SPM prediction, the comparisons are shown in Figure 5.6. According to the SPM prediction, the RCS decreases rapidly for large correlation lengths. From 37.5° to 60°, the backscatter coefficient drops by 40 dB, while the simulated result drops by 10 dB. This difference shows the limitation of the model for predicting surfaces with a large correlation length at a large incident angle as discussed in Section 2.7.

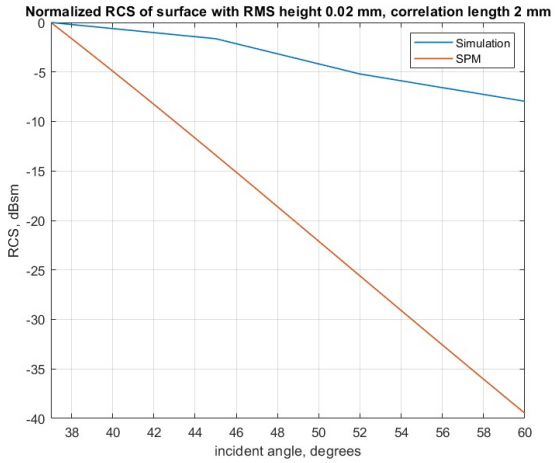

Figure 5.6: Comparison of horizontal RCS and SPM prediction for $\sigma = 0.02$ mm and $l = 2$ mm

Figure 5.7 and 5.8 show the difference of the averaged scattered field of the rough surface and the flat surface case at an incident angle of 45° and 60°. For the incident angle of 45°, the backscattered power for the rough surface is larger than the flat surface by approximately 10 dB. In contrast, for the incident angle of 60°, the backscattered power for the two cases is close to each other. The similarity between the backscattered power for the rough surface and the flat surface at 60° indicates that the backscattered field of the rough surface case is not mainly caused by the backscattered power due to the roughness of the surface but by the diffraction from the surface edge instead. As a consequence, the RCS result is influenced and thus does not agree with the SPM theory.

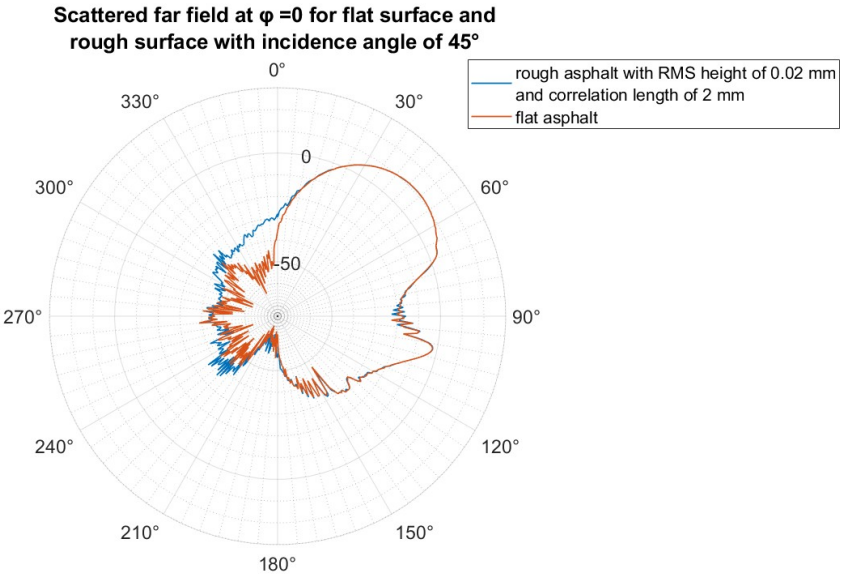

Figure 5.7: Far field at $\phi = 0$ with horizontal source incident at 45° of the three rough and flat surface cases

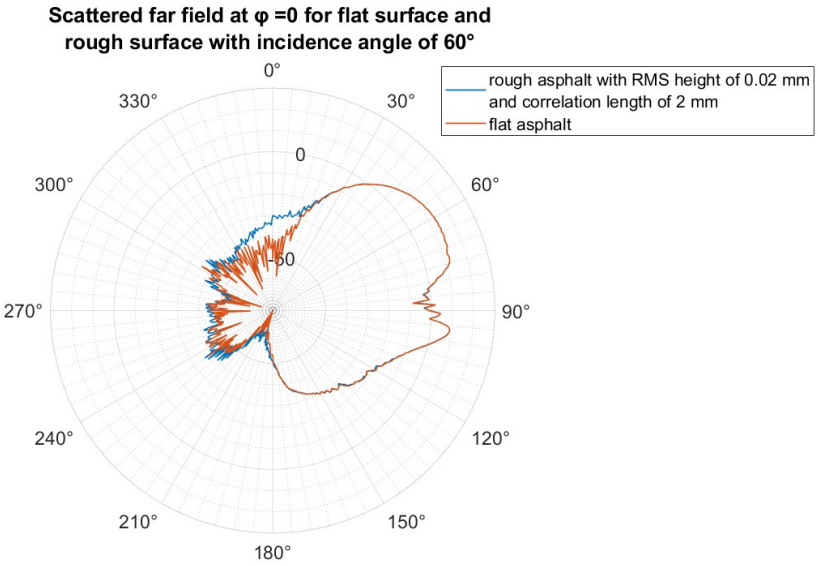

Figure 5.8: Far field at $\phi = 0$ with horizontal source incident at 60° of the three rough and flat surface cases

5.2. Conclusion

In this chapter, the designed numerical model is validated by the analytical model of SPM. The verification is done within the validation region of the SPM, in which the slope and RMS height of the surface are small. In the case of a surface with a small slope and a small correlation length, the simulation results show good agreement with the SPM prediction. However, in the case of a surface with a small slope and a large correlation length, the dynamic range and rate of decay as a function of incident angle of the RCS from the simulation results are different from the SPM prediction. This disagreement is the result of the model limitations described in Section 2.7. The comparison of the results of the rough surface and the flat surface indicates that the accuracy of the model is determined by whether the backscattering is strongly interfered with by the diffraction of the surface or not. The verification results show that the designed model can make accurate predictions for the scattering of rough surfaces, although with limited accuracy in the case of a complicated combination of incident angle and surface roughness. When the diffraction level is less than the backscattered power, the results from the designed model are accurate. However, the results become less accurate when the diffraction level is comparable to or larger than the backscattered power.

6

Conclusion

6.1. Summary and conclusions

In this project, the asphalt surface scattering properties at 76 GHz are studied. The scattering from rough surfaces is affected by many factors. Because the roughness of asphalt is comparable to the wavelength, it is difficult to have a comprehensive solution for the scattering problem of this kind of surface. In order to resolve this issue, a novel numerical procedure is created in the electromagnetic simulation software suite FEKO. This model takes into account the influence of the dielectric medium, the statistics of the roughness, and polarization and orientation of the electromagnetic wave source. Due to the usage of the commercial electromagnetic software FEKO, the developed model can be easily modified for other similar studies, such as scattering on a surface with different properties or in a different medium.

Using the model developed, for the first time, the scattering properties of very rough surfaces with a large slope are analyzed. For a very rough surface, the simulation results show that the RCS at both vertical and horizontal polarizations at incident angles ranging from 37.5° to 60° are close to each other with the maximum difference between the HH and VV components is 3 dB. Moreover, the RCS of such a very rough surface decreases by 3 dB and 7 dB as the incident angle increases. The difference between the co-polar and cross-polar components is about 10 dB at the incident angle of 37.5° and increases to 14 dB at 60°.

The RCS dependence on surface roughness of RMS height is studied at the incident angle of 45°. The simulation results show that the surface RCS increases for all four components with the RMS height increases. Compared to a surface with an RMS height of 0.02 mm, the RCS value for a surface with an RMS height of 2mm increased by 30 to 40 dB. When the RMS height is 0.02 mm, the difference between the two polarization components is 3 dB for HH and VV and 12 dB for HV and VH. This difference between RCS at orthogonal polarizations approaches zero when the RMS height is 2 mm.

Furthermore, based on the developed single-layer model, a multiple-layer model is developed to investigate the impact of an additional layer of water on the asphalt surface. The simulation results show that the flat water layer increases specular reflection and that the backscattered power is reduced by 20 dB to 25 dB compared to the case of the single asphalt layer.

Due to the restricted computational resources available, the model developed has limitations. The limitations are analyzed based on the current distribution and the size of footprint. In the case of slightly rough surfaces with a large correlation length and large incident angle, the scattered result is impacted by the strong edge diffraction that reduces the simulation dynamic range to 40 dB. The model is validated by the analytical model SPM. In the case of surfaces with a small correlation length, the simulation results are consistent with the analytical model, whereas the expected deviation from the SPM is observed for surfaces with a small roughness and a large correlation length.

6.2. Recommendations for future research

As discussed in Section 2.7, there are several limitations to the numerical model. To solve these issues, an achievable solution is to increase the size of the surface further to suppress the current level at the surface edge. Moreover, the footprint size can be increased, and more realizations can be used to achieve a more accurate average result.

The second recommendation relates to calibrating vertical sources. Due to the asymmetry of the source radiation, the footprint of the two polarization sources is not the same, with only the rotation being changed. To resolve such

an error, the orientation of the vertical source needs to be calibrated to be identical to the horizontal source. This could not be done in this project due to time limits.

The third recommendation is to use a new source with a narrower beam width. The beam width of the source used in this project is 24.83°, a narrower beam width could simulate a plane incident wave better and reduce the phase error of surface current. An achievable way is to increase the size of the dipole array further. Figure 6.1 shows the radiation pattern of a binomial dipole array with 41 elements in each dimension and the dipole array used in this project. The new source has a smaller beam width of 9.57°. More simulations should be run with the new source to obtain more accurate results. However, this could not be finished in time for this project.

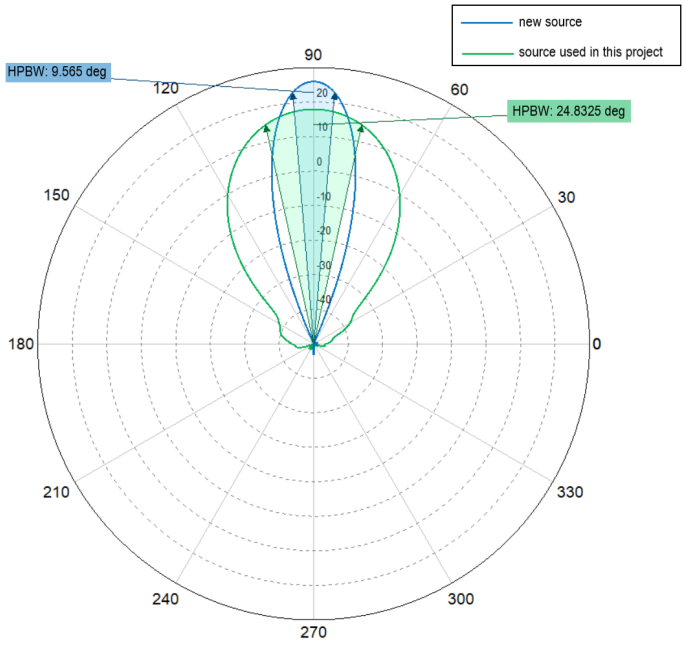

Figure 6.1: Radiation pattern of the new source and the source used in this project

References

[1] *Gladheid door ijzel*. https://www.knmi.nl/kennis-en-datacentrum/waarschuwingen/gladheid.

[2] Aleksandr Bystrov et al. "Sensors for Automotive Remote Road Surface Classification". In: *2018 IEEE International Conference on Vehicular Electronics and Safety (ICVES)*. 2018, pp. 1–6. DOI: 10.1109/ICVES.2018.8519499.

[3] FT Ulaby et al. "Statistical properties off the Mueller matrix off distributed targets". In: *IEE Proceedings F (Radar and Signal Processing)*. Vol. 139. 2. IET. 1992, pp. 136–146.

[4] H. Rudolf et al. "Road condition recognition using microwaves". In: *Proceedings of Conference on Intelligent Transportation Systems*. 1997, pp. 996–999. DOI: 10.1109/ITSC.1997.660609.

[5] Ville Viikari et al. "Automotive radar technology for detecting road conditions. Backscattering properties of dry, wet, and icy asphalt". English. In: *5th European Radar Conference, EuRAD 2008*. 5th European Radar Conference 2008 ; Conference date: 30-10-2008 Through 31-10-2008. United States: IEEE Institute of Electrical and Electronic Engineers, 2008, pp. 276–279.

[6] Ville V Viikari et al. "Road-condition recognition using 24-GHz automotive radar". In: *IEEE transactions on intelligent transportation systems* 10.4 (2009), pp. 639–648.

[7] K. Sarabandi et al. "Modeling and measurements of scattering from road surfaces at millimeter-wave frequencies". In: *IEEE Transactions on Antennas and Propagation* 45.11 (1997), pp. 1679–1688. DOI: 10.1109/8.650080.

[8] Abdulrahman Alaqeel et al. "Sub-Millimeter Wave Automotive Radars for Road Assessment Applications". In: *IGARSS 2022 - 2022 IEEE International Geoscience and Remote Sensing Symposium*. 2022, pp. 1257–1259. DOI: 10.1109/IGARSS46834.2022.9883212.

[9] Peter Asuzu et al. "Road condition identification from millimeter-wave radar backscatter measurements". In: *2018 IEEE Radar Conference (RadarConf18)*. 2018, pp. 0012–0016. DOI: 10.1109/RADAR.2018.8378522.

[10] Pengxiang Xie et al. "Terahertz Wave Propagation Characteristics on Rough Surfaces Based on Full-Wave Simulations". In: *Radio Science* 57.6 (2022). e2021RS007385 2021RS007385, e2021RS007385. DOI: https://doi.org/10.1029/2021RS007385. eprint: https://agupubs.onlinelibrary.wiley.com/doi/pdf/10.1029/2021RS007385. URL: https://agupubs.onlinelibrary.wiley.com/doi/abs/10.1029/2021RS007385.

[11] Jun Cheng Wei et al. "Surface and volumetric scattering by rough dielectric boundary at terahertz frequencies". In: *2016 IEEE International Geoscience and Remote Sensing Symposium (IGARSS)*. 2016, pp. 3680–3682. DOI: 10.1109/IGARSS.2016.7729953.

[12] Mai Alissa et al. "The Effect of Rough Surface Statistics on Diffuse Scattering at Terahertz Frequencies". In: *2019 European Conference on Networks and Communications (EuCNC)*. 2019, pp. 118–122. DOI: 10.1109/EuCNC.2019.8802032.

[13] James A Ogilvy et al. *Theory of wave scattering from random rough surfaces*. 1991.

[14] Christophe Bourlier et al. "One-and two-dimensional shadowing functions for any height and slope stationary uncorrelated surface in the monostatic and bistatic configurations". In: *IEEE Transactions on Antennas and Propagation* 50.3 (2002), pp. 312–324.

[15] AK Fung et al. "An integral equation method for rough surface scattering". In: *Proceedings of the International Symposium on multiple scattering of waves in random media and random surfaces*. 1986, pp. 701–714.

[16] E.S. Li et al. “Modeling and measurement of scattering from rough asphalt surfaces at millimeter-wave frequencies”. In: *IEEE Antennas and Propagation Society International Symposium. 1998 Digest. Antennas: Gateways to the Global Network. Held in conjunction with: USNC/URSI National Radio Science Meeting (Cat. No.98CH36*. Vol. 2. 1998, 974–977 vol.2. DOI: 10.1109/APS.1998.702112.

[17] Jin Au Kong et al. *Scattering of electromagnetic waves: numerical simulations*. John Wiley & Sons, 2004.

[18] Altair Feko 2021. *Far Fields and Receiving Antennas*. URL: https://2021.help.altair.com/2021/feko/topics/feko/user_guide/output_file/farfields_receving_ant_feko_r.htm.

[19] Kane Yee. “Numerical solution of initial boundary value problems involving maxwell’s equations in isotropic media”. In: *IEEE Transactions on Antennas and Propagation* 14.3 (1966), pp. 302–307. DOI: 10.1109/TAP.1966.1138693.

[20] Chi-Hou Chan et al. “Electromagnetic scattering of waves by random rough surface: A finite-difference time-domain approach”. In: *Microwave and Optical Technology Letters* 4.9 (1991), pp. 355–359.

[21] Kyung Pak et al. “Combined random rough surface and volume scattering based on Monte Carlo simulations of solutions of Maxwell’s equations”. In: *Radio Science* 28.3 (1993), pp. 331–338. DOI: https://doi.org/10.1029/93RS00275. eprint: https://agupubs.onlinelibrary.wiley.com/doi/pdf/10.1029/93RS00275. URL: https://agupubs.onlinelibrary.wiley.com/doi/abs/10.1029/93RS00275.

[22] S H Lou et al. “Application of the finite element method to Monte Carlo simulations of scattering of waves by random rough surfaces: penetrable case”. In: *Waves in Random Media* 1.4 (1991), pp. 287–307. DOI: 10.1088/0959-7174/1/4/006. eprint: https://doi.org/10.1088/0959-7174/1/4/006. URL: https://doi.org/10.1088/0959-7174/1/4/006.

[23] Patrik Hermansson et al. “A review of models for scattering from rough surfaces”. In: *Linköping: FOI-Swedish Defence Research Agency* (2003).

[24] Heather Lawrence et al. “Evaluation of a Numerical Modeling Approach Based on the Finite-Element Method for Calculating the Rough Surface Scattering and Emission of a Soil Layer”. In: *IEEE Geoscience and Remote Sensing Letters* 8.5 (2011), pp. 953–957. DOI: 10.1109/LGRS.2011.2131633.

[25] R.L. Wagner et al. “Monte Carlo simulation of electromagnetic scattering from two-dimensional random rough surfaces”. In: *IEEE Transactions on Antennas and Propagation* 45.2 (1997), pp. 235–245. DOI: 10.1109/8.560342.

[26] Elisabet Rufas Talamàs. “Surface Scattering Analysis Evaluation of asphalt scattering properties”. 2022.

[27] Yue Chen. “Extra Project: Surface Scattering”. 2022.

[28] R.T. Marchand et al. “On the use of finite surfaces in the numerical prediction of rough surface scattering”. In: *IEEE Transactions on Antennas and Propagation* 47.4 (1999), pp. 600–604. DOI: 10.1109/8.768797.

[29] Yu Liang et al. “A Study of Scattering From Rough Surface With Different Scale of Roughness Based on the Efficient Numerical Strategies”. In: *IEEE Access* 8 (2020), pp. 217877–217882. DOI: 10.1109/ACCESS.2020.3041160.

[30] Xin-Bo He Wei Tian Bing Wei. “A novel domain decomposition-finite difference time domain method for composite scattering from a target above rough surface”. In: *Waves in Random and Complex Media* (2019).

[31] Yu Li et al. “Backscattering from Fractal Rough Surfaces Under Tapered Wave Illumination”. In: *IGARSS 2018 - 2018 IEEE International Geoscience and Remote Sensing Symposium*. 2018, pp. 2131–2134. DOI: 10.1109/IGARSS.2018.8519577.

[32] Dirk P. Kroese et al. “Why the Monte Carlo method is so important today”. In: *WIREs Computational Statistics* 6.6 (2014), pp. 386–392. DOI: https://doi.org/10.1002/wics.1314. eprint: https://wires.onlinelibrary.wiley.com/doi/pdf/10.1002/wics.1314. URL: https://wires.onlinelibrary.wiley.com/doi/abs/10.1002/wics.1314.

[33] *Special Software and Computers*. http://radar.ewi.tudelft.nl/Facilities/soft.php.

[34] Altair Feko 2022.3. *Altair Feko User Guide*. URL: https://help.altair.com/feko/pdf/Altair_Feko_User_Guide.pdf.

[35] *DelftBlue: the TU Delft supercomputer*. https://www.tudelft.nl/dhpc/system.

[36] Hossein Zamani et al. “Scattering by a three dimensional buried object beneath multilayered rough surface illuminated by a collimated microwave Gaussian pulse”. In: *AEU - International Journal of Electronics and Communications* 123 (2020), p. 153329. DOI: https://doi.org/10.1016/j.aeue.2020.153329. URL: https://www.sciencedirect.com/science/article/pii/S1434841120304362.

[37] Nannan Chen. “Millimetre wave propagation and scattering phenomena for automotive radar”. 2016.

A

FEKO setup for the numerical model

This section explains the setup for the model in the FEKO.

A.1. Single asphalt model

1. After creating a new blank project, the rough surface model is imported.

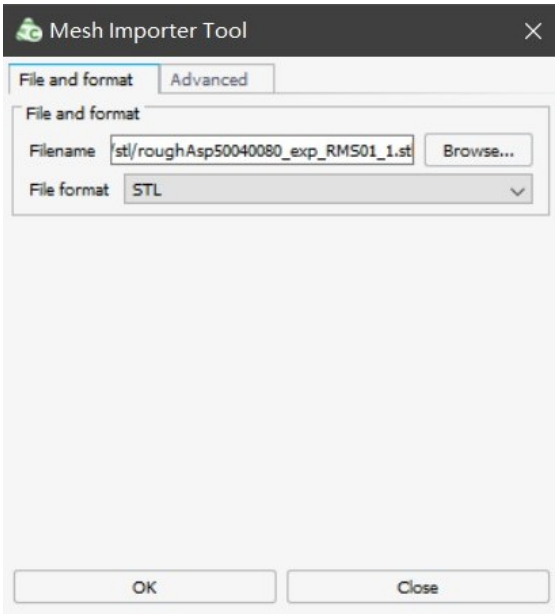

2. Define asphalt medium and the mesh properties.

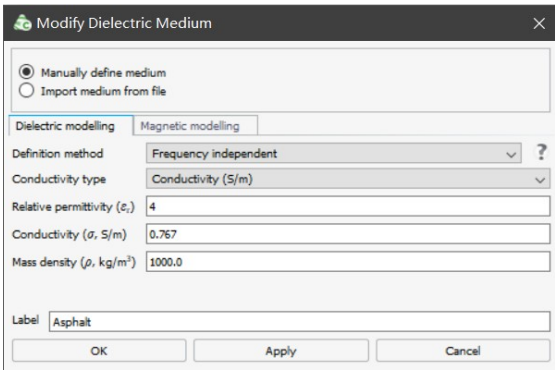

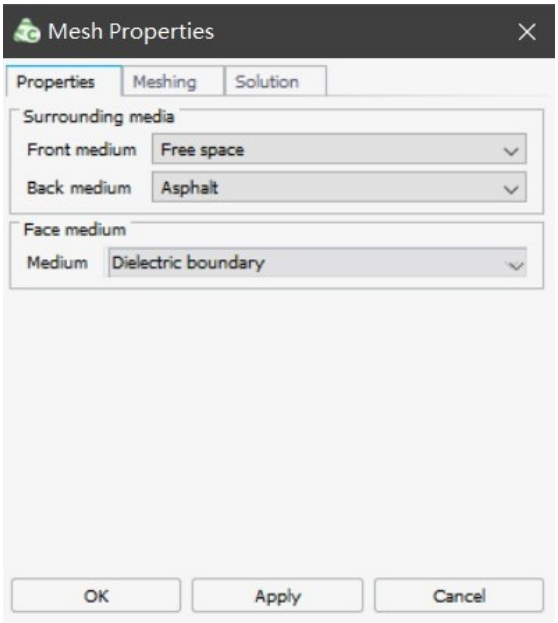

3. Import equivalent spherical mode source file and define source orientations. The variables dx and dz are the source shifts for the incidence angle, where $dx = d\sin(\theta), dz = d\cos(\theta)$, d is the distance between the source and surface and θ is the incidence angle. The rotation angle is the incident angle, for a rotation angle of 0°, the source incident is at 45°.

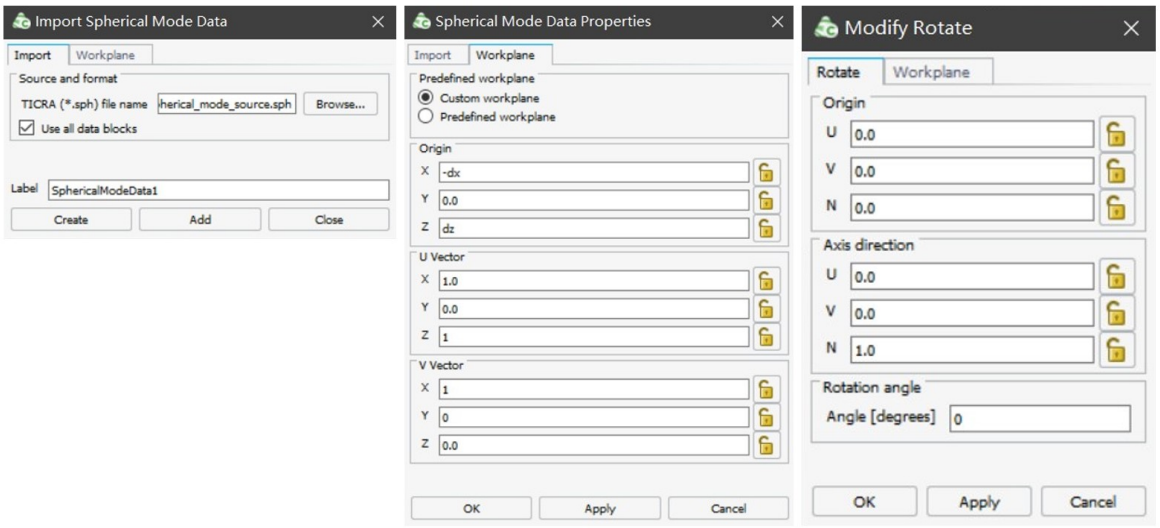

4. Before setting up the meshing rules, the frequency of the model is defined in the frequency menu, then meshing rules are defined in the ”Modify mesh” tab.

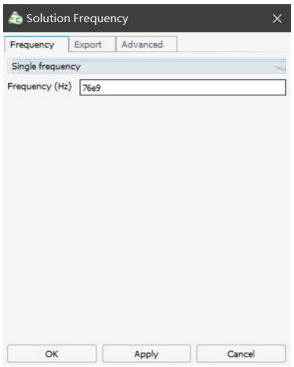

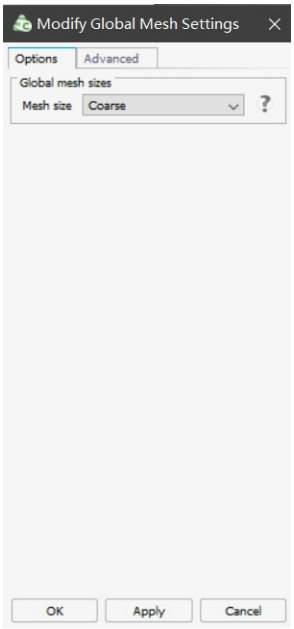

5. To enable the re-meshing of the imported surface model by FEKO, the option of use model mesh needs to be disabled. The simulation mesh can then be automatically generated by FEKO.

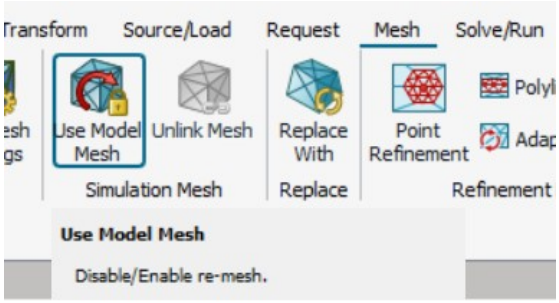

6. The solver is defined in the solver settings. The MLFMM solver is enabled, and the iterative solve and SPAI preconditioner are selected in the advanced settings.

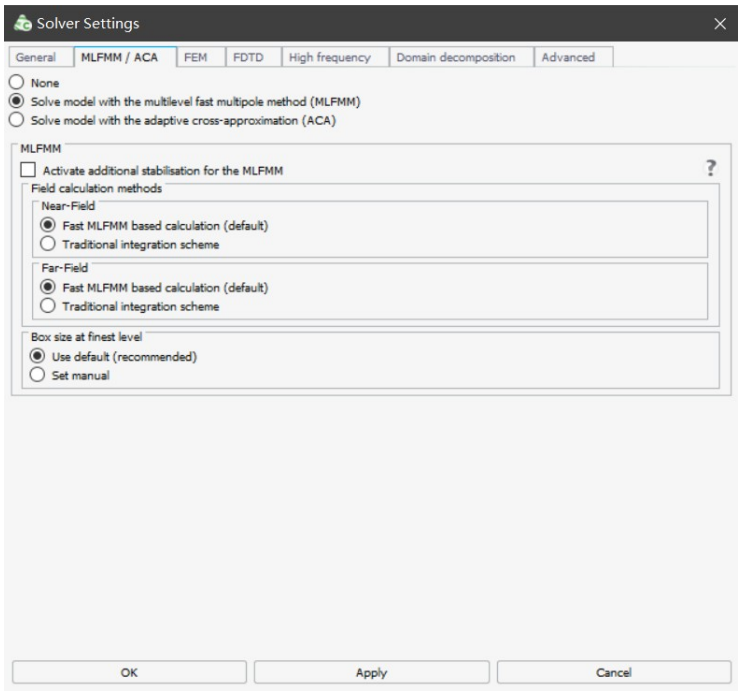

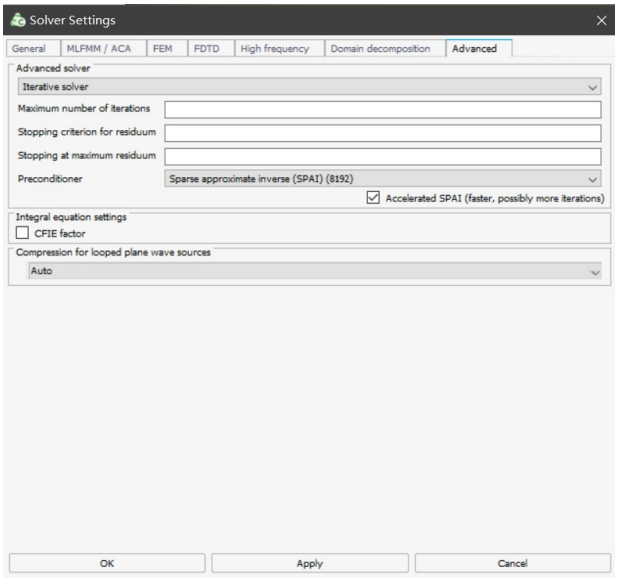

7. A far-field request is added to obtain the scattered field. The requst is defined in spherical coordinates, with $\theta \in (0°,\ 180°)$ and $\phi \in (0°,\ 360°)$. The result is sampled by a $1°$ step.

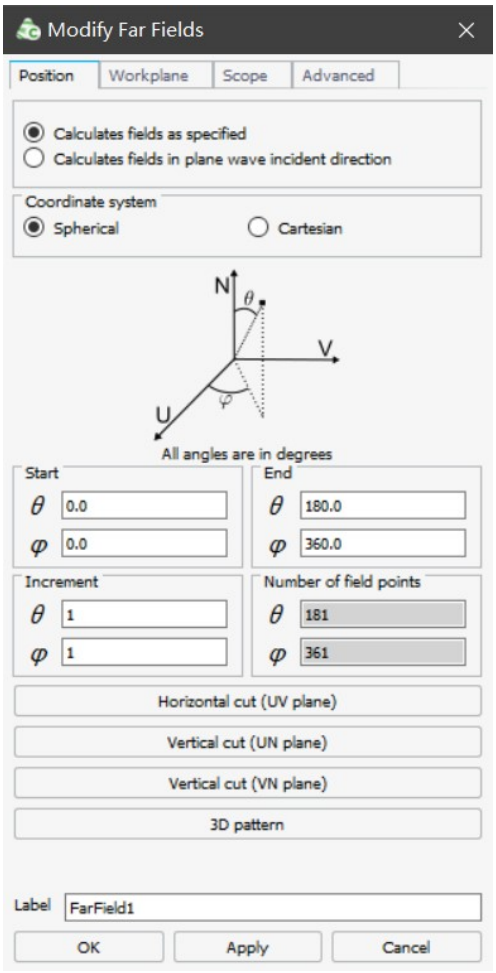
Modify Far Fields
Position
Workplane
Scope
Advanced
Calculates fields as specified
Calculates fields in plane wave incident direction
Coordinate system
Spherical
Cartesian
N
θ
V
U
φ
All angles are in degrees
Start
θ 0.0
φ 0.0
End
θ 180.0
φ 360.0
Increment
θ 1
φ 1
Number of field points
θ 181
φ 361
Horizontal cut (UV plane)
Vertical cut (UN plane)
Vertical cut (VN plane)
3D pattern
Label FarField1
OK
Apply
Cancel

8. Start simulation by clicking ”Feko solver”.

A.2. Multiple asphalt and water model

1. Import the asphalt and water layer model and define mesh properties following the same steps described in step 1 in Section A.1 and define the medium properties for water.

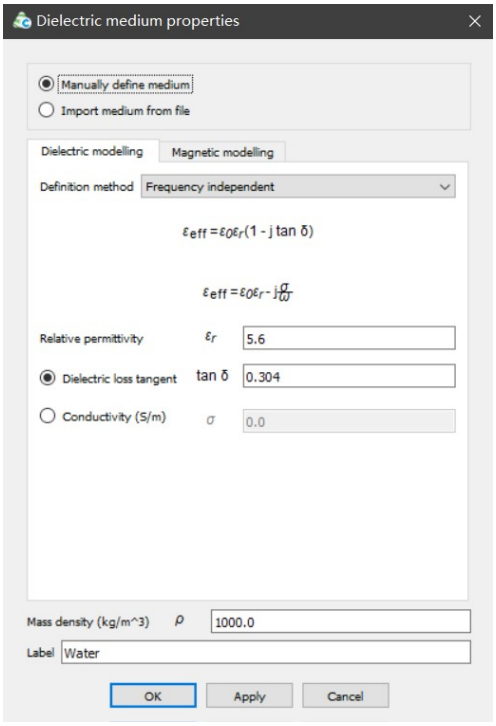

2. For the asphalt layer, define a cut plane at $x = 0, y = 0, z = -30$ mm and switch to the top view of the model.

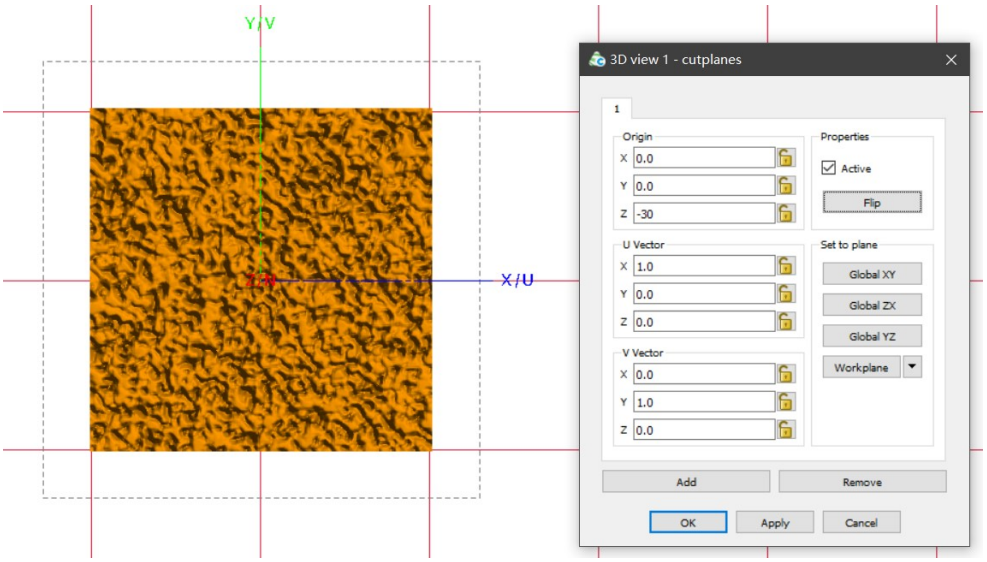

3. Select the mesh elements on the top surface by rectangular selection and picking the mesh element option. Rename the top surface as ”SurfaceMesh1”. The top surface mesh is deleted after renaming it.

4. For the water layer model, the mesh elements of the bottom surface are selected and renamed as ”SurfaceMesh1” following the same steps as step 1 to step 3. The cut plane is defined at $x = 0, y = 0, z = 5$ mm.
5. The three mesh elements are merged together by the option ”Merge meshes”. The mesh properties of the merged mesh are defined. The water and asphalt layer properties are defined as the same as in step 2 in Section A.1, the bottom surface properties are defined by the water and the asphalt.

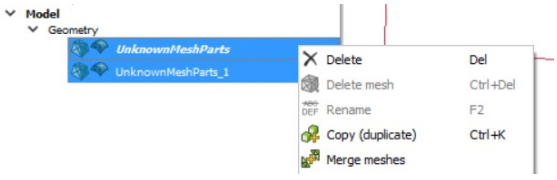

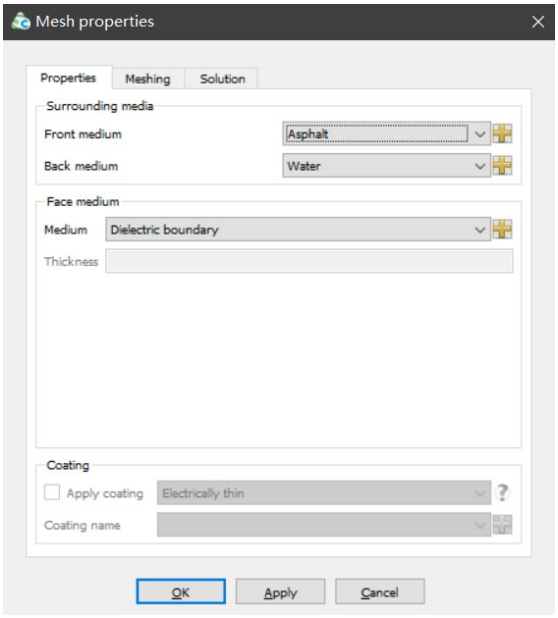

6. The rest of the simulation settings including the source orientation, the meshing rules, the solver settings, and far field request are defined as shown in step 3 to step 7 in Section A.1. The simulation is started by clicking the ”Feko solver”.

B

Simulation scripts

This section presents the scripts for running simulations on DelftBlue.

B.1. Model meshing script

```
#!/bin/bash
#
#SBATCH --job-name="prefeko"
#SBATCH --partition=compute
#SBATCH --time=05:00:00
#SBATCH --ntasks=1
#SBATCH --cpus-per-task=2
#SBATCH --mem-per-cpu=50000M
#SBATCH --account=research-eemcs-me

module load feko/2022.2.1
export LC_ALL=en_US.UTF-8

# Run cadfeko_batch and prefeko
cd file path
srun file name > output_cadfeko.log
srun file name > output_prefeko.log
```

B.2. Model solver script

```
#!/bin/bash
#
#SBATCH --job-name="feko_mem"
#SBATCH --partition=memory
#SBATCH --time=08:00:00
#SBATCH --ntasks=48
#SBATCH --nodes=1
#SBATCH --cpus-per-task=1
#SBATCH --mem=749G
#SBATCH --account=research-eemcs-me

module load feko/2022.2.1
export LC_ALL=en_US.UTF-8

# Create a machines file based on the node list allocated
hostlist=$(scontrol show hostname $SLURM_JOB_NODELIST)
cpulist=$(echo $SLURM_JOB_CPUS_PER_NODE | awk 'BEGIN {FS = ","} {for (i=1; i<=NF; i++) ...
    {s=split($i,a,"x"); if (s>1) for (j=1; j<=a[2]; j++) {print a[1]+0} else print $i}}')
paste <(printf "%s\n" "${hostlist[@]}") <(printf "%s\n" "${cpulist[@]}") | awk '{print ...
    $1":"$2}' > machines.feko

export FEKO_MACHFILE="machines.feko"

cd file path
```

```
runfeko file name --use-job-scheduler > output.log
killall runfeko
```

C

Matlab code

The Matlab code for processing the simulation results is shown in this section.

```
clear all
clc
close all

%   Near field result at (0,0,0)
E0 = 6.83137e+6;
H0 = 18133.6;
P0 = 0.5 * E0 * H0; % incident power density

%  Illuminated area size for different incidence angle
area_37_5 = [0.0085 0.0088 0.0088 0.0086];
area_45 = [0.0094 0.0094 0.0094 0.0093];
area_52_5 = [0.0104 0.0105 0.0105 0.0104];
area_60 = [0.0119 0.0117 0.0117 0.0116];

filevariable= 'RMS002'
area = area_37_5;% size of illuminated area
index1 = 324;
index2 = 325;

%Read TXH data (rough surface)
files_txh = dir(['**/corr04_RMS002/' filevariable '/H/*.ffe']); % file path
for i = 1:length(files_txh)

    filename = files_txh(i).name;
    filepath = [files_txh(i).folder '/' filename]; %get full file path

    Data_h = readffe(filepath,17);

    txh_farfield(i,:,:) = Data_h;
end

% Read TXV data (rough surface)
files_txv = dir(['**/' filevariable '/V/*.ffe']);
for j = 1:length(files_txv)
    filename = files_txv(j).name;
    filepath = [files_txv(j).folder '/' filename];

    Data_v = readffe(filepath,17);

    txv_farfield(j,:,:) = Data_v;
end

% Take phi cut for txh (rough)
for n = 1: size(txh_farfield,1)

    ff_h = squeeze(txh_farfield(n,:,:));
    ff_h_cut = takephi0cut(ff_h);

    txh_phi_cut(n,:,:) = ff_h_cut;
```

```
end

%  Take phi cut for txv (rough)
for nn = 1: size(txv_farfield,1)

    ff_v = squeeze(txv_farfield(nn,:,:));
    ff_v_cut = takephi0cut(ff_v);

    txv_phi_cut(nn,:,:) = ff_v_cut;
end

% Calculate the averaged gain
txh_gain = squeeze( txh_phi_cut(:,:,9));
txh_gain_mean = mean(txh_gain);
txh_gain_mean_db = db(txh_gain_mean,"power");

txv_gain = squeeze( txv_phi_cut(:,:,9));
txv_gain_mean = mean(txv_gain);
txv_gain_mean_db = db(txv_gain_mean,"power");

% plot averaged far field in polar plot
thetaaxis = 0:1:360;
figure
polarplot( deg2rad(thetaaxis([1:end 1 ])), txh_gain_mean_db([1:end 1]),'LineWidth',1)
hold on
polarplot( deg2rad(thetaaxis([1:end 1])), txv_gain_mean_db([1:end 1]),'LineWidth',1)
rlim([-60-5 20+10])
title('Averaged far fields at phi=0, dB')
legend('rough asphalt -TxH','rough asphalt-TxV')
grid minor
pax = gca;
pax.ThetaDir= 'clockwise'
pax.ThetaZeroLocation = 'top';

% Calcule the theta and phi components of electric field in the case of horizontal source
txh_Etheta = txh_phi_cut(:,:,3) + 1j * txh_phi_cut(:,:,4);
txh_Ephi = txh_phi_cut(:,:,5) + 1j * txh_phi_cut(:,:,6);

% Calculate averaged Bistatic RCS in the case of horizontal source
for m = 1: size(txh_Etheta,1)
    RCS_HH(m,:) = 4*pi * ( abs(txh_Ephi(m,:) .* conj(txh_Ephi(m,:))) / P0 ) / area(1);
    RCS_HV(m,:) = 4*pi * ( abs(txh_Etheta(m,:) .* conj(txh_Etheta(m,:))) / P0 ) / area(2);
end

RCS_HV_mean = mean(RCS_HV,1);
RCS_HH_mean = mean(RCS_HH,1);

% Calcule the theta and phi components of electric field in the case of vertical source
txv_Etheta = txv_phi_cut(:,:,3) + 1j * txv_phi_cut(:,:,4);
txv_Ephi = txv_phi_cut(:,:,5) + 1j * txv_phi_cut(:,:,6);

% Calculate averaged Bistatic RCS in the case of vertical source
for mm = 1: size(txv_Etheta,1)
    RCS_VH(mm,:) = 4*pi * ( abs(txv_Ephi(mm,:) .* conj(txv_Ephi(mm,:))) / P0 ) / area(3);
    RCS_VV(mm,:) = 4*pi * ( abs(txv_Etheta(mm,:) .* conj(txv_Etheta(mm,:))) / P0 ) / ...
        area(4);
end

RCS_VV_mean = mean(RCS_VV,1);
RCS_VH_mean = mean(RCS_VH,1);

% Save averaged far ield and Bistatic RCS data
FF_cut = [thetaaxis;txh_gain_mean;txv_gain_mean]';
PV = [thetaaxis;PV_HH_mean;PV_HV_mean;PV_VH_mean;PV_VV_mean]';
RCS = [thetaaxis;RCS_HH_mean;RCS_HV_mean;RCS_VH_mean;RCS_VV_mean]';
savename = [filevariable '_win.mat'];
save(savename,"FF_cut","RCS")

figure
plot(thetaaxis,10*log10(abs(RCS_HH_mean)),LineWidth=1)
hold on
```

```
plot(thetaaxis,10*log10(abs(RCS_HV_mean)),LineWidth=1)
hold on
plot(thetaaxis,10*log10(abs(RCS_VH_mean)),LineWidth=1)
hold on
plot(thetaaxis,10*log10(abs(RCS_VV_mean)),LineWidth=1)
grid on
xlabel('Theta, degrees')
ylabel('Bistatic RCS, dB/m^2')
legend('HH','HV','VH','VV')

% Calculate the averaged, maximum, minmum, and standard error of the RCS
[max_HH,¬]=max(0.5 * ( RCS_HH(:,index1)+ RCS_HH(:,index2) ));
[min_HH,¬]=min(0.5 * ( RCS_HH(:,index1)+ RCS_HH(:,index2) ));
ave_HH = 0.5 * (RCS_HH_mean(:,index1) + RCS_HH_mean(:,index2));
std_HH = std(0.5 * ( RCS_HH(:,index1)+ RCS_HH(:,index2) ))/sqrt(size(RCS_HH,1));
RCS_HH_bs = [max_HH min_HH ave_HH std_HH];

[max_HV,¬]=max(0.5 * ( RCS_HV(:,index1)+ RCS_HV(:,index2) ));
[min_HV,¬]=min(0.5 * ( RCS_HV(:,index1)+ RCS_HV(:,index2) ));
ave_HV = 0.5 * (RCS_HV_mean(:,index1) + RCS_HV_mean(:,index2));
std_HV = std(0.5 * ( RCS_HV(:,index1)+ RCS_HV(:,index2) ))/sqrt(size(RCS_HV,1));
RCS_HV_bs = [max_HV min_HV ave_HV std_HV];

[max_VH,¬]=max(0.5 * ( RCS_VH(:,index1)+ RCS_VH(:,index2) ));
[min_VH,¬]=min(0.5 * ( RCS_VH(:,index1)+ RCS_VH(:,index2) ));
ave_VH = 0.5 * (RCS_VH_mean(:,index1) + RCS_VH_mean(:,index2));
std_VH = std(0.5 * ( RCS_VH(:,index1)+ RCS_VH(:,index2) ))/sqrt(size(RCS_VH,1));
RCS_VH_bs = [max_VH min_VH ave_VH std_VH];

[max_VV,¬]=max(0.5 * ( RCS_VV(:,index1)+ RCS_VV(:,index2) ));
[min_VV,¬]=min(0.5 * ( RCS_VV(:,index1)+ RCS_VV(:,index2) ));
ave_VV = 0.5 * (RCS_VV_mean(:,index1) + RCS_VV_mean(:,index2));
std_VV = std(0.5 * ( RCS_VV(:,index1)+ RCS_VV(:,index2) ))/sqrt(size(RCS_VV,1));
RCS_VV_bs = [max_VV min_VV ave_VV std_VV];

% Save the RCS data
savename1 = [filevariable '_RCS_backsc.mat'];
save(savename1,"RCS_HH_bs","RCS_HV_bs","RCS_VH_bs","RCS_VV_bs")

function ff = readffe(fullpath,firstline)
file_fullpath = fullpath;
fid = fopen(file_fullpath,'rt');
Data = textscan(fid,'%f %f %f %f %f %f %f %f %f', ...
    "HeaderLines",firstline,'CollectOutput',true);
fclose(fid)
Data = cell2mat(Data);
ff = Data;
ff(:,7:9) = 10 .^ (ff(:,7:9) / 10); % convert db to linear scale
end
```